

---

# Semi-Infinite Laguerre Functions for Wind Turbine Wake Modeling

Thomas Sebastiaan Lokken

04/2022-02/2023

# Semi-Infinite Laguerre Functions for Wind Turbine Wake Modeling

Master of Science Thesis  
March 19, 2023

**Author:** T.S. Lokken TU Delft - Master student  
**Committee:** Dr. N.G.W. Warncke Siemens Gamesa - Loads engineer  
Dr. D.A.M. de Tavernier TU Delft - Assistant professor  
Prof. Dr. D.A. von Terzi TU Delft - Chair of Wind Energy Technology

March 19, 2023

---



# Summary

With an increased demand for renewable energy wind farms, their efficiency receives growing attention from both the industry and academics. Mitigating wake interaction effects in wind farms is one of the ways wind farms could increase their efficiency. Control techniques to increase wake reenergizing are currently under development, however, are being held back by a lack of available medium-fidelity wake modeling methods. To sufficiently support developments in the wind industry, the wake model should yield an axial wind profile that can be used for load calculations for the downstream wind turbine and assess its energy production. Moreover, for the model to be useful in the research effort the method must either show an increase in accuracy or a decrease in time-cost. Finally, the model is desired to include the effects of wake control techniques in later iterations outside the scope of this research.

This thesis investigates medium-fidelity models for wind turbine wake control techniques, with an exploratory study into applying a semi-infinite spectral method with an adjusted Laguerre basis to wind turbine wake modeling. The wake model used in this research is an altered version of the Ainslie wake model. To model the wake model a spectral method with Laguerre functions for the basis is employed in the radial direction and a marching scheme with a piecewise linear basis for the basis in the downstream direction. The potential benefits of spectral methods are lower rank systems and spectral convergence. The adjusted Laguerre functions used for this research naturally fit the boundary conditions for the wake model. At the start of the domain, a Dirichlet boundary condition is applied with fitted Laguerre functions to the result of a blade element simulation.

The results did not account for wake expansion and diffused the wake much sooner than physical. The implementation of the explicit formulation for the triple product integral hindered higher-order simulations, disabling research into simulations for domains much higher than 11 radial modes. The errors for the different conserved quantities are significantly higher than they should be. From the verification efforts, a relation can be observed between the number of radial modes in the domain with respect to the number of radial modes used for the inflow, which suggests that the model should use much higher numbers of radial modes than this implementation allowed.

Overall, this thesis demonstrates some of the risks accompanying semi-infinite Laguerre functions to axisymmetric flow cases. Furthermore, it lays the foundation for further investigation and highlights the potential improvements for future spectral methods with Laguerre basis functions. Improving the implementation of the explicit triple product integral should yield improvements for the model immediately. To include wake control for the model, the next step would be to remove the simplification of the eddy viscosity equation. This may not just be used to cover the dynamic induction control, but may also lead to more physical dissipation of the wake.

# Preface

I do not believe in truly independent success, rather I think all works are in a way team efforts. It is, therefore, that I would like to shine a light on the people who have helped me through the past months. My direct team exists of Delphine de Tavernier and Norbert Warncke. Your knowledge and patience have astounded me. Truly, I cannot imagine a better team for the work I have had to complete. The past 10 months were a rush of learning experiences leading up to what this work, and I, have become and I would gladly have done it exactly the same way again.

Of course, a team in such a personal project as a thesis consists of more than just supervisors. My fellow student Giulia Gatti has helped me drag myself through many letdowns and has often managed to cheer me right back up when the project let me down. Additionally, my housemates have always been there to help me weigh the options and decisions required to finish this work.

A special thanks goes to my parents, who have supported me, regardless of their lack of connection to the content matter. At last, I would like to thank my most unique supporter, Sanna Gerdes. You have offered a listening ear for my whining and problem descriptions, reacting with supportive words and potential solutions. Your proofreading has helped me elevate this work to a new level.

Finally, I would like to mention my colleagues at the Siemens Gamesa office, who have been nothing but welcoming and friendly to me. Except for at the foosball table, where I have spent many of my office hours playing away.

# Nomenclature

## Latin symbols

$a$	Axial induction factor	—
$a'$	Radial induction factor	—
$b$	Projection basis function	—
$dA$	Area measure	$m^2$
$dV$	Volume measure $m^3$	
$D$	Rotor diameter	$m$
$f$	General function notation	—
$H$	Hermite polynomial	—
$h_t$	Size of the time step	$s$
$h_{xx}$	Cubic Hermite spline function	—
$\mathbb{I}$	Identity matrix	—
$I$	Integral product	—
$I_{amb}$	Ambient turbulence intensity	—
$J$	Jacobian matrix	—
$L$	Laguerre polynomial or operator	—
$N$	Number of steps	—
$N_r$	Highest order radial mode	—
$\mathcal{O}$	Convergence rate	—
$\tilde{r}$	Non-dimensional radius $2r/D$	—
$r$	Radial dimension	$m$
$R_w$	Wake expansion	$m$
$t$	Time or the piecewise dimension for the cubic Hermite spline	$s$
$\mathbf{u}$	Vector of velocity coefficients in the downstream direction	$m/s$
$\tilde{u}$	Non-dimensional velocity $U/U_\infty$	—

$U$	Velocity in downstream direction	$m/s$
$U_\infty$	Incoming velocity	$m/s$
$\mathbf{v}$	Vector of velocity coefficients in the radial direction	$m/s$
$V$	Velocity in radial direction	$m/s$
$\tilde{x}$	Non-dimensional downstream position $2x/D$	—
$x$	Downstream dimension	$m$

### Greek symbols

$\varepsilon$	Relative error	—
$\varepsilon_t$	Relative error in time step	—
$\zeta$	Hermite function	—
$\delta$	Kronecker delta	—
$\partial$	Partial differential operator	—
$\gamma$	Resulting integral constant for the Jacobi orthogonality	—
$\bar{\nu}_T$	Averaged eddy viscosity	$m^2/s$
$\nu_t$	Eddy viscosity	$m^2/s$
$\nu_T$	Eddy viscosity	$m^2/s$
$\vec{n}$	Normal vector	—
$\Omega$	General domain notation	$m^2/s$
$\partial\Omega$	Boundary of an element within the domain or the boundary of the domain	$m^2/s$
$\psi$	Laguerre function	—
$\rho$	Alternative radial dimension notation	$m$
$\theta$	Azimuthal dimension	—

### Subscripts

$k, q, m$	Radial mode
$l$	Left-sided element in marching scheme
$m$	Projection element
$r$	Right-sided element in marching scheme

### Superscripts

$\alpha$	The $\alpha$ -coefficient used in the definition of the Laguerre equations or the $\alpha$ -coefficient used in the Jacobi polynomials corresponding to the generating function
$\beta$	The $\beta$ -coefficient used in the Jacobi polynomials corresponding to the generating function
$k$	Integer corresponding to the order of the Laguerre function
$i$	Iterator for the Newton-Rhapson method or indication of step in time
$n$	Integer corresponding to the order of the Hermite function
$\omega$	Weighting function
'	Derivative with respect to the only dependent or an iterator of a similar sum

### Abbreviations

ALT	Actuator Line Theory
BEM	Blade Element Momentum
DIPC	Dynamic Individual Pitch Control
DIC	Dynamic Induction Control
FE	Finite Element
LES	Large Eddy Simulation
RANS	Reynolds Averaged Navier Stokes
SEM	Spectral Element Method

# List of Figures

- 2.1 Schematic diagram of wind turbine wake structure taken from Uchida et al. [2021]. Do note the Gaussian far-wake region. . . . . 10
- 2.2 The schematic of the force decomposition along a blade element . . . . . 12
- 2.3 Results of the improved tip loss correction compared to the Glauert method by Shen et al. [2005] . . . . . 13
- 2.5 Convergence of 4th-order finite difference and Fourier-collocation differentiation processes (Shen et al. [2011]). . . . . 16
- 2.6 Linear basis function used for finite element method in axial direction . 25
  
- 3.1 Comparison of the eigenvalues for the radial derivative diffusion term with respect to a scaled quadratic function. All elements adhere to being nonzero. . . . . 35
  
- 4.1 The results for the tests of the radially discretized diffusion term with an adjusted Laguerre function support. . . . . 44
- 4.2 The visualization of the velocity coefficients and the velocity profile at higher errors . . . . . 45
- 4.3 Error results for a fixed number of radial modes for the domain with differing numbers of radial modes used to model the inflow. The simulations were performed with 8 radial modes in the domain. . . . . 48
  
- 5.1 Flow of the script with its iterative convergence scheme colorized. . . . . 52
- 5.2 Boundary inflow projected onto basis functions for different numbers of radial modes . . . . . 54
- 5.3 The resulting wakes both for a prescribed viscosity of  $8e^{-3}$  . . . . . 55
- 5.4 The results of the wake model with the eddy viscosity equation implemented for each downstream step, for  $I_{amb} = 3e - 2$  . . . . . 56
- 5.5 Errors in the final results for the conservation of mass and momentum. The domain . . . . . 57
  
- B.1 Schematic of cubic Hermite spline finite element discretization. . . . . 68

B.2	The schematics of the boundaries for the FE discretization. The basis functions used for the FE approach are the cubic Hermite splines. . . .	71
-----	---	----

# List of Tables

- 5.1 Scaling parameters and the corresponding error for different numbers of radial modes fitted to the inflow conditions. . . . . 53
- 5.2 Highest error in the symmetric relation for this implementation of the Laguerre explicit triple product integral. The highest error is computing one fixed order and going over the other modes up to 15. The first 4 orders are not included, because they are close to machine precision . . . 58

# Contents

<b>Summary</b>	<b>i</b>
<b>Preface</b>	<b>iii</b>
<b>Nomenclature</b>	<b>iv</b>
<b>List of Figures</b>	<b>vii</b>
<b>List of Tables</b>	<b>viii</b>
<b>Table of Contents</b>	<b>ix</b>
<b>1 Introduction</b>	<b>1</b>
1.1 Research Objective and Questions . . . . .	2
1.2 Outline of the Report . . . . .	4
<b>2 State of the Art</b>	<b>5</b>
2.1 Instationary Models . . . . .	5
2.1.1 Large-Eddy Simulation . . . . .	5
2.1.2 Actuator Line Theory . . . . .	7
2.2 Stationary Models . . . . .	8
2.2.1 Reynolds Averaged Navier Stokes . . . . .	8
2.2.2 Ainslie Wake Model . . . . .	9
2.2.3 Blade Element Momentum Theory . . . . .	12
2.3 Numerical Methods . . . . .	14
2.3.1 Domain Partitioning . . . . .	14
2.3.2 Jacobi Basis . . . . .	17
2.3.3 Bessel Functions . . . . .	17
2.3.4 Hermite Functions . . . . .	18
2.3.5 Laguerre Functions . . . . .	21
2.3.6 Marching Scheme . . . . .	24

2.4	Conclusion . . . . .	25
<b>3</b>	<b>Two-Dimensional Modeling</b>	<b>27</b>
3.1	Mass Continuity . . . . .	27
3.1.1	Natural Radial Basis Functions . . . . .	27
3.1.2	The System of Mass Continuity . . . . .	29
3.2	Momentum Equation . . . . .	31
3.2.1	Diffusion Term . . . . .	31
3.2.2	Nonlinear Terms . . . . .	36
3.2.3	Nonlinear Solver . . . . .	40
<b>4</b>	<b>Verification</b>	<b>41</b>
4.1	Diffusion Equation . . . . .	41
4.2	Full System of Equations . . . . .	44
<b>5</b>	<b>Wake Analysis</b>	<b>51</b>
5.1	The Modelled Boundary Conditions . . . . .	51
5.2	Wake Expansion . . . . .	53
5.3	Eddy Viscosity Effects . . . . .	55
5.4	Conservation Error . . . . .	56
<b>6</b>	<b>Conclusion and Recommendation</b>	<b>59</b>
6.1	Conclusion . . . . .	59
6.2	Recommendations . . . . .	61
<b>A</b>	<b>The One-Equation System</b>	<b>63</b>
<b>B</b>	<b>Hermite Spline Implementation</b>	<b>67</b>
B.1	Hermite Spline Marching . . . . .	68
B.2	Hermite Spline Finite Elements . . . . .	69
	<b>Bibliography</b>	<b>73</b>

[This page is intentionally left blank]

# Chapter 1

## Introduction

To reach the emission reduction target set by the Paris agreement, many industries need to hasten the transition to a carbon-free future. The energy sector is a critical actor in this transition, through the realization of energy transition schemes (CAT [2022]). In Europe alone, the energy capacity increase due to wind energy is estimated to increase by 116 GW from 2022-2026, of which a quarter will be sourced offshore (Europe [2022]). Clustering wind turbines in wind farms offshore is a common practice to lower the expenses of putting the turbines in place, as well as the costs of running and maintaining the electricity grid and the turbines themselves.

Downstream of a wind turbine, the wind flow has a lower velocity and an increased turbulence intensity (Vermeer et al. [2003]), thereby hampering the efficiency of clustered wind turbines. This region of lower velocity and increased turbulence is what is referred to as the wake. Wake interaction of wind turbines comes with lower power production (Barthelmie and Jensen [2010]) and an increase in fatigue loads (Thomsen and Sørensen [1999]). Keeping the cost of the energy transition as low as possible motivates research in the direction of wake aerodynamics. This research aims to lessen the thresholds that currently impede wind farm clustering.

Methods to mitigate wake effects must be accompanied by a wake model to assess their corresponding effectiveness. The range of fidelity of such models is large and, consequently, the difference in the time spent simulating differs from minutes to days (RANS and LES from Sexbierum benchmarking study by Göçmen et al. [2016]). Less complex aspects of wind farm design, such as annual energy production, may be sufficiently supported by the lowest-order models. Contrastingly, the structural properties of downstream wind turbines may require higher-order models, to compute accurate fatigue loading and accurate aeroelastic loading (Adams et al. [2016]).

For many years the focus of wind energy research has been put on optimizing the design of single wind turbines. However, with the increasing number of wind farms in strictly limited areas, the demand for optimization of the power per unit area has gone

up. This optimization is not a straightforward process as it requires a strong interface between the two disciplines of control technique and aerodynamics. A periodic excitation of the flow is achieved by applying a superimposed low-frequency sinusoidal signal on the blade pitch angles (Frederik et al. [2020b], van der Hoek et al. [2022]). This technique is known as dynamic induction control (DIC).

Another method stemming from the same cross of disciplines is the dynamic individual pitch control (DIPC). This method does not just enhance turbulent mixing by increasing the turbulence downstream, but, induces additional wake meandering (Frederik et al. [2020a]). Wake meandering refers to the phenomenon of the wake propagating in a zigzag shape downstream, resembling the meandering of rivers. Individual pitch control leads to a helical shape of the wake propagation, thereby enhancing the turbulent mixing of the wake.

This paper contains exploratory research into possible numerical methods to model the wake in the case of dynamic induction control or dynamic individual pitch control. Though it does not contain an exact method to model the wake for any wake control techniques, it does point research in the direction of medium-fidelity modeling of such wakes. Using numerical methods, which have not been thoroughly applied to wind turbine wake modeling, may yield improvements in the computational cost and accuracy of the method, granted a correct implementation.

The foundation of numerical improvements comes from a comprehensive understanding of what exactly it is that should be modeled. The target for this model is the lowest-order model for the wake control techniques, which supports the aero-elastic load calculations by Adams et al. [2016]. Improving load calculations will help the research efforts and save precious engineering hours for development. The load calculations need the axial velocity profile of the wake, setting the first crucial requirement. The second requirement follows from the implementation target, modeling on a wind farm level. To realistically achieve farm level calculations, the computational cost should remain low. Later versions should allow for extensions to compute distinct results for periodic time inputs or azimuthal inputs.

## 1.1 Research Objective and Questions

This section provides the structure of this research. From the targets set in the introduction, comes the main research objective, which is as follows:

*This thesis aims to lay the foundation for computationally cheap modeling of State-of-the-Art wake control techniques with Ainslie's wake model by implementing semi-infinite Laguerre functions.*

The objective contains the two requirements as set in the introduction of this chapter. The result of the Ainslie wake model contains the necessary inputs for the load calculations. Furthermore, the semi-infinite Laguerre functions offer a potential numerical improvement from the typical numerical methods applied. The evaluation of said Laguerre functions is part of the main focus of this research effort, where its implementation forms the foundation for the research questions.

Firstly, regarding the applicability of the implementation of the wake modeling technique for the specific flow case, an advantage of the specific numerical method may be a very high-order of convergence. This is, however, not the case for every modeling instance. The question thus arises if the high-order of convergence aligns with the wind turbine wake.

Within the boundaries of this question, it may be worthwhile to evaluate the results and consider if the Laguerre functions are not ill-suited for the problem. This can be assessed for many aspects of the model (e.g., inflow modeling, governing equations, and the shape of the problem).

Secondly, an interesting aspect to take up in this research is the realistic applicability of the model. Generally, put: will the result support research efforts into the effects of wind turbine wakes? For the result to be useful, the time cost to run the model should be kept low and surpass the methods currently used in the industry. The optimization of the result falls outside of the scope of this research, but system ranks and computation costs for unoptimized scripts should yield useful insights.

Nevertheless, if the result of the research yields an inaccurate, but, fast model, it may still not see any use outside this research. For an erroneous model, the possible root of the error is particularly interesting. The most straightforward way of checking this accuracy is by comparing it to other models and assessing the error in conservation properties. The second main research question and its sub-questions follow from this second set of concerns.

**Q-1 Is a spectral method with Laguerre basis functions in the radial direction an adequate choice for axisymmetric wind turbine wake modeling?**

**Q-1.1** How close to spectral convergence is the model for the modeling of wind turbine wakes?

**Q-1.2** Are the Laguerre functions a good pick for the problem?

**Q-2 Will the axisymmetric wind turbine wake model contribute to the field of wind turbine wake modeling?**

**Q-2.1** Is the time-cost to run the full model within industry standards?

**Q-2.2** Is the accuracy of the full model satisfactory?

## **1.2 Outline of the Report**

The report is structured in the following way. Chapter 2 will provide the reader insight into the state-of-the-art models which could be used for wake modeling. Different modeling techniques in wind-turbine wake modeling are discussed and the numerical methodology is introduced. Chapter 3 focuses on the numeric implementation for the developed wake model, whereas, chapter 4 concerns itself with the verification of the implementation. In chapter 5 the model's results are shown and discussed. Finally, in chapter 6 the research is concluded and recommendations for future research efforts are provided.

# Chapter 2

## State of the Art

Within wake modeling, it is common to divide the wake into two distinct sections. The near- and the far-wake. The definitions of these distinctions are not set in stone and may vary per study. Typically, the near-wake is where the upstream rotor's properties can still be discriminated. The most correct definition of the far-wake is the flow section beyond what is defined as the near-wake. For this domain, the wake is dominated by the power properties of the upstream wind turbine.

This chapter will outline the most relevant wake modeling techniques and numerical methods for this research. The models and methods do not account for a complete set of all the possible ways of wind turbine wake modeling. The first section considers itself with instantaneous models section 2.1. Next, the time-averaged wake models are discussed in section 2.2. Finally, section 2.3 covers the numerical methods considered for the implementation of the wake models.

### 2.1 Instationary Models

The first distinction considers the instationary models. Models which approximate the solution of the problem for each step in time. The strength of these methods is that highly unsteady flow properties may be modeled accurately.

#### 2.1.1 Large-Eddy Simulation

Large-Eddy Simulation (LES) is the most sophisticated method to be realistically implemented in state-of-the-art models. Though Direct Numerical Simulations (DNS) may yield more accurate results, the computational cost to perform DNS makes it infeasible for many flow cases.

Fundamental to LES is the treatment of turbulence. Including turbulence in the Navier-Stokes equations demands solving for a big spectrum of length and time scales. All length and time scales affect the flow fields, however, larger length scales possess stronger kinetic energy, thus altering the flow to a higher extent. LES applies a low-pass filter to the turbulent scales, DNS to the large eddy scales, and modeling for the smaller eddy scales.

There are many different modeling techniques that can be used for subgrid-scale modeling, however, these are not included in the scope of this literature study, since LES is the slowest method discussed for the modeling of the wakes. The momentum equation for the LES is (Sedaghatizadeh et al. [2018]):

$$\frac{\partial(\rho\bar{u}_i)}{\partial t} + \frac{\partial(\rho\bar{u}_j\bar{u}_i)}{\partial x_j} = \frac{\partial\sigma_{ij}}{\partial x_j} - \frac{\partial\bar{p}}{\partial x_i} - \frac{\partial\tau_{ij}}{\partial x_j} \quad (2.1)$$

Where  $\bar{u}$  is the resolved velocity,  $\sigma_{ij}$  the molecular viscosity stress tensor, and  $\tau_{ij}$  the subgrid-scale stress. The subgrid-scale stress was defined by Leonard [1975] as consisting of three components. The first component, the Leonard stress tensor (L), corresponds to the effect of large-eddies on each other. The smaller interactions between the modeled subgrid eddies are then captured by the Reynold subgrid tensor (R). The last component corresponds to the interaction of the small eddies with the large eddies and is thoughtfully named the cross-stress tensor C, the expression for subgrid-scale stress then becomes  $\tau_{ij}$ :

$$\tau_{ij} = L_{ij} + C_{ij} + R_{ij} \quad (2.2)$$

With the momentum equation defined, and the mass continuity as:

$$\frac{\partial\rho}{\partial t} + \frac{\partial}{\partial x_i}(\rho\bar{u}_i) = 0 \quad (2.3)$$

The system may be solved.

LES has been proven to work well for wind turbine interaction and flowfield modeling by Porté-Agel et al. [2011], hence showcasing the applicability of LES for wake modeling of wind farms.

Moreover, Munters and Meyers [2018] suggest LES can be used for dynamic induction and yaw control of individual turbines for wind-farm power maximization. Dynamic induction and yaw control will put similar constraints on the system as DIPC.

LES may be regarded as the state-of-the-art high-fidelity method. The cost of the LES, however, reflects its high accuracy. The required refinement is one of the leading sources of computational cost. Choi and Moin [2011] approximate the required grid refinement of the wall-flow by:  $N_{DNS} \sim Re_{Lx}^{13/7}$ . This comes down to  $7.4 \times 10^{12}$  grid points for the blade of an offshore wind turbine at an incoming velocity of 19 m/s and

a max chord of 8.5 [m]. By means of parallelizing the problem, the simulation may be optimized. Regardless, LES will result in a costly model.

### 2.1.2 Actuator Line Theory

To circumvent the enormous cost belonging to the LES modeling of offshore wind turbines. Sørensen and Shen [2002] came up with an alternative to the modeling of the blades by including them as concentrated force points acting on the flow. Donso reduces the cost of a LES for offshore wind turbines. This is achieved by discretizing the blade in two-dimensional actuator points (N,M). Each actuator point is then subjugated to the blade element theory as seen in figure 2.2. The force vector( $f_{2D}$ ) corresponding to the actuator points is a function of the resulting lift and drag. This force vector should then be expressed in the flow grid's respective x, y, and z axes. This force vector is a point force approximation, which in itself is not a physical representation of the force distribution in the flow. To circumvent this unphysical aspect, the force vector shall be projected on the surrounding flow field by means of a Gaussian kernel function,  $\eta$  in equation (2.5) (Sørensen and Shen [2002]). In this equation,  $\underline{r}$  represents the distance vector from the grid point to the actuator element, and  $\epsilon$  governs the width of the Gaussian.

The force of the actuator point on the grid point,  $f$  in equation (2.4), contributes to the body force in the momentum equation for that grid point. The force on the grid point will act in the opposite direction of the force of the airfoil, thus the contribution to the body force is negative.

$$\underline{f}(x_{grid}) = - \sum_N \sum_M \underline{f}_{2D}(x_{N,M}, y_{N,M}, z_{N,M}, t) \eta_{N,M} \quad (2.4)$$

$$\eta_{N,M} = \frac{1}{\epsilon^3 \pi^{3/2}} \exp \left[ \left( - \frac{|\underline{r}|}{\epsilon} \right)^2 \right] \quad (2.5)$$

Archer and Vassel-Be-Hagh [2019] applied ALT in combination with LES to investigate wake steering, showcasing the capabilities of asymmetric inflow modeling. ALT is also used to qualitatively assess experimental finds (Howland et al. [2016]). ALT is typically considered a high-order method and is used as a high-order modeling technique, however, the method is still relatively costly when compared with the stationary models. Moving towards stationary models comes at the cost of losing the time-dependent flow properties (Afgan et al. [2013]).

## 2.2 Stationary Models

The models discussed in this section model the flow as a time-independent phenomenon. This means that the dimension of time periods, or inclusion of different time increments, no longer affects the outcome of the models. The results can therefore be interpreted as an averaged flow. The computational time is much lower compared to the instationary models, due to the convenience of disregarding the time dimension.

### 2.2.1 Reynolds Averaged Navier Stokes

The concept fundamental to Reynolds Averaged Navier Stokes (RANS) is the Reynolds decomposition of the Navier Stokes momentum equation. By breaking up the velocity into a time-averaged and a fluctuating term, the instantaneous turbulence may still be modeled, regardless of Reynolds-averaging. Rewriting the velocity component and providing the notation for these variables yields (Wilcox [1994]):

$$u(x, t) = \bar{u}(x) + u'(x, t) \quad (2.6)$$

$$\bar{u}(x) = \lim_{T \rightarrow \infty} \frac{1}{T} \int_t^{t+T} u(x, t) dt \quad (2.7)$$

$$\bar{u}'(x) = \lim_{T \rightarrow \infty} \frac{1}{T} \int_t^{t+T} u'(x, t) dt = 0 \quad (2.8)$$

The incompressible Navier Stokes are what brings the RANS into the discussion in the first place. Plugging the equation for  $u(x,t)$  in the mass continuity(2.9) and momentum continuity(2.10), yields a Navier Stokes formulation expressed in terms of time-averaged ( $\bar{u}$ ) and fluctuating ( $u'$ ) velocity (Wilcox [1994]):

$$\frac{\partial \bar{u}_i}{\partial x_i} = 0 \quad (2.9)$$

$$\rho \frac{\partial \bar{u}_i}{\partial t} + \rho \bar{u}_j \frac{\partial \bar{u}_i}{\partial x_j} = -\frac{\partial \bar{p}}{\partial x_i} + \frac{\partial}{\partial x_j} (2\mu S_{ji} + \overline{\rho u'_j u'_i}) \quad (2.10)$$

This is a fully time-averaged two-dimensional Navier Stokes equation, where the subscripts indicate the dimension depending on what dimension the momentum is taken in. For instance, taking the momentum in the x-direction  $i=x, j=y$ . The equation is not yet closed. The  $\overline{\rho u'_j u'_i}$ , the Reynolds stress term, still requires modeling. Doing this analytically yields 22 unknowns, thereby, completely tipping the equation's balance resulting in an indeterminate system. This problem is known as the closure problem.

Applying the Boussinesq hypothesis allows the equations to be determinant again. By introducing the definitions of eddy viscosity( $\nu$ ) and turbulent kinetic energy, a foundation was laid to solve the RANS equations. Long after the appearance of eddy viscosity and the turbulent kinetic energy, the closure problem was solved. With equations for the eddy viscosity, turbulent kinetic energy, and dissipation rate, the set of equations became determinant again (Wilcox [1994]). These models are known as the Turbulence Energy Equation models and are commonly classified by the number of equations employed to close the set of equations.

RANS, generally, shows improvement in computational cost with respect to LES. The RANS equations may be further simplified to decrease the amount of modeling required for the system of equations.

### 2.2.2 Ainslie Wake Model

The Ainslie wake model is derived from the two-dimensional RANS equations formulated in cylindrical coordinates. By neglecting gravity and pressure, and applying the assumptions for incompressible, stationary, and axisymmetric flow, the general equation for the Ainslie wake model can be expressed. The final step to achieve the Ainslie wake notation is to apply the Boussinesq assumption to the axisymmetric viscous force term as described in equation (2.11)(Kim et al. [2018]). The non-velocity components in equation (2.11) are the kinematic viscosity,  $\nu$ , dynamic viscosity,  $\mu$ , and the air density  $\rho$ . The averaged velocity is expressed by  $u$ , in the axial direction, and  $v$ , in the radial direction. Plugging equation (2.11) into the momentum equation equation (2.12), leads to the following formulation of the momentum equation(2.13) by Ainslie [1988]:

$$-uv = \frac{\mu}{\rho} \frac{\partial u}{\partial r} = \nu \frac{\partial u}{\partial r} \quad (2.11)$$

$$u \frac{\partial u}{\partial x} + v \frac{\partial u}{\partial r} = -\frac{1}{r} \frac{\partial}{\partial r} \left( r \overline{uv} \right) \quad (2.12)$$

$$u \frac{\partial u}{\partial x} + v \frac{\partial u}{\partial r} = \frac{1}{r} \nu \frac{\partial}{\partial r} \left( r \frac{\partial u}{\partial r} \right) \quad (2.13)$$

What sets the classical eddy viscosity by Ainslie [1988] aside, is that it requires no additional equation to be modeled. The eddy viscosity model consists of two components. The first component describes the turbulent mixing due to turbulence within the shear layer of the wake. The turbulence within the shear layer is computed from the length ( $l_w(x)$ ) and velocity ( $U_w(x)$ ) scales describing the wake shear layer. The second component describes the effect of ambient turbulence in the atmosphere on wake mixing. Combining the two components allows for the eddy viscosity as seen in equation (2.14).

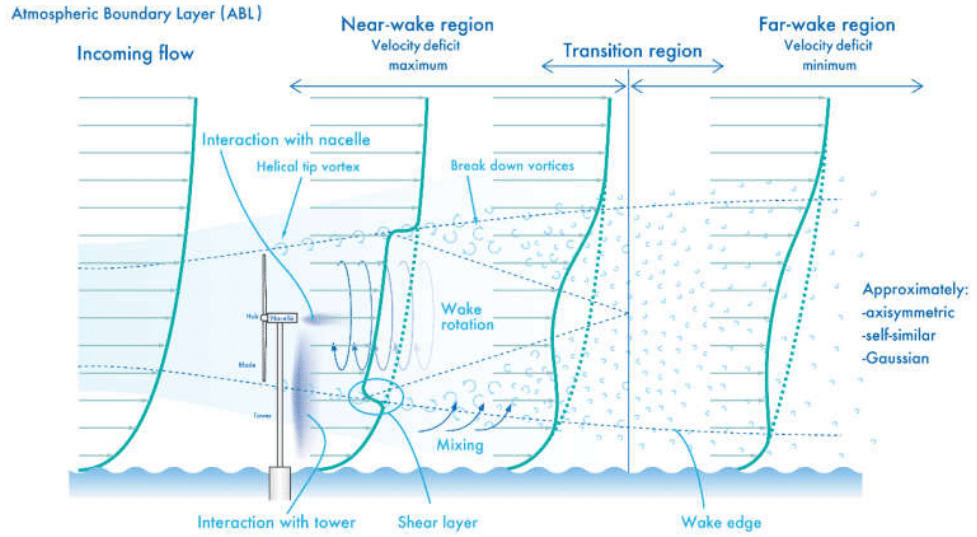


**Figure 2.1:** Schematic diagram of wind turbine wake structure taken from Uchida et al. [2021]. Do note the Gaussian far-wake region.

$$\nu = l_w(x)u_w(x) + \nu_a \quad (2.14)$$

The length and velocity scales are taken to be proportional to the wake width, which may be determined utilizing the mass continuity equation, and the velocity difference  $u_\infty - u_c$  across the wake shear layer; these scales are therefore characteristic of the downstream distance  $x$  and independent of  $r$ . To model the wake, Ainslie [1988] starts the model 5 diameters downstream of the wind turbine, recognizing the model's inability to capture the near-wake behavior. For this implementation, the focus lies on the far-wake, loss of flow structures at the start of the domain does not need to pose an issue. Modern implementations of derived models such as by Larsen et al. [2012], or Keck et al. [2014].

Currently, it is unknown how these assumptions will function under the flow conditions of the DIC or the DIPC. Specifically, the axisymmetric flow profile is a troublesome aspect, as there are a few flow properties that will result in errors for this assumption. Firstly, wind turbine wakes are never axisymmetric due to the atmospheric shear layers. The inflow wind velocity will always come in with a nonuniform wind profile, leading to a lower wind speed closer to the earth. This effect and the resultant wake shape can be seen in figure 2.1. This figure also reflects the benefit of the Ainslie wake approach. The far-wake shows a velocity profile resembling a Gaussian distribution, which can be captured well by an axisymmetric model.

By modeling DIPC employing an axisymmetric time-averaged flow model, the initial

model may be extended to include an azimuthal flow component. This could be enough to capture some of the asymmetric flow properties. To fully model turbulent structures such as tip vortices, time-averaged flow models are generally not a good option, since the average of the fluctuation may as well be zero. However, the effect of DIPC on the wake may influence the average outcome of the flow. When the average flow properties are affected, the Ainslie wake could make a sufficiently accurate model.

Picotto et al. [2018] have combined modeling of collective pitch control with yaw steering, using the Ainslie wake model. This model is in line with the ambitions set for this research and proves the feasibility of, at the very least, the modeling of induction control. Ainslie's eddy viscosity wake model is chosen to be applied for the flow case, as the lowest-order physics-based model, which supports enough flow properties to motivate the research. Eliminating the assumption of low circumferential velocity and time averaging may yield satisfactory results for DIOC. By only introducing time dependence, the method may be well applicable to symmetric induction control without extra effort. Alternatively, eliminating the no pressure gradient assumption could improve the outcome for both cases.

Computationally, the Ainslie wake model, with its corresponding assumptions, represents a state-of-the-art medium-fidelity wake model adhering to the requirements needed to support the implementation of a 'wake atlas' (Adams et al. [2016]). The following equation is used for the modeling of Ainslie's eddy viscosity:

$$\frac{2\nu_T}{DU_\infty} = 0.023F_1(\tilde{x})I_{amb}^{0.3} + 0.016F_2(\tilde{x})\frac{R_w(\tilde{x})}{D} \left(1 - \frac{U_{min}(\tilde{x})}{U_\infty}\right) \quad (2.15)$$

This equation is opted for as it is the industrial standard (Commission [2019]) and the focus of this research is on the numerical implementation. Equation (2.15) is fitted to the 'Egmond aan zee' Wind farm by Larsen et al. [2012]. Providing the following filter functions:

$$F1 = \begin{cases} \left(\frac{\tilde{x}}{8}\right)^{\frac{3}{2}} - \frac{\sin(2\pi\tilde{x}^{3/2})}{2\pi} & 0 \leq \tilde{x} < 8 \\ 1 & 8 \leq \tilde{x} \end{cases}$$

$$F2 = \begin{cases} 0.0625 & 0 \leq \tilde{x} < 4 \\ 0.025\tilde{x} - 0.0375 & 4 \leq \tilde{x} < 12 \\ 0.00105(\tilde{x} - 12)^3 + 0.025\tilde{x} - 0.0375 & 12 \leq \tilde{x} < 20 \\ 1 & 20 \leq \tilde{x} \end{cases}$$

Where  $\tilde{x}$  is the non-dimensionalized  $x$ ,  $\tilde{x} = \frac{2x}{D}$ . The definition used for the wake radius ( $R_w$ ) is where the wake is 95% of the incoming velocity.

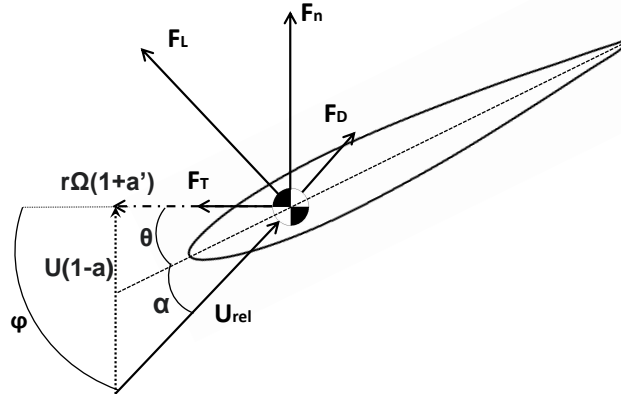


Figure 2.2: The schematic of the force decomposition along a blade element

### 2.2.3 Blade Element Momentum Theory

The Blade Element Momentum (BEM) theory is the consolidation of two theories, momentum theory, and blade element theory.

Momentum theory relies on the actuator disk theory. The simplest case of the actuator disk is a constantly loaded permeable disk of infinitesimal thickness. A force field is distributed over the actuator disk representing the force field of the rotor. As a consequence, the flow expands. The expanded downstream flow, also known as the wake, will have a lower velocity than the incoming velocity. This velocity reduction in momentum theory is described with the induction factor, by  $U_{wake} = U_{\infty}(1 - 2a)$  (Burton et al. [2011]). Similarly, the momentum theory in azimuthal direction  $U_{\theta} = \Omega r(1 + 2a')$  (Burton et al. [2011]). These velocities are the wake modeling of the classical BEM theory.

Blade element theory concerns itself with the decomposition of the forces of a blade cross-section based on the inflow angle ( $\phi$ ) and the perceived velocity ( $U_{rel}$ ), similar to figure 2.2. The section twist ( $\theta$ ), the incoming velocity ( $U$ ), and the rotational velocity ( $\Omega$ ) are fixed properties for the design. From the inflow angle and the section twist, the angle of attack ( $\alpha$ ) may be calculated. From the angle of attack, the lift and drag coefficient may be calculated with the help of the lift and drag polars for the airfoil. The last symbols in the figures are the induction factor ( $a$ ) and the tangential induction factor ( $a'$ ).

The annuli are to be independent of one another in the BEM model. The independence from an annulus comes from the assumption that there is no interaction between the separate annuli and that there is no flow between the elements. These assumptions lead to quite a significant error for many of the annuli. For instance, at the tip of the

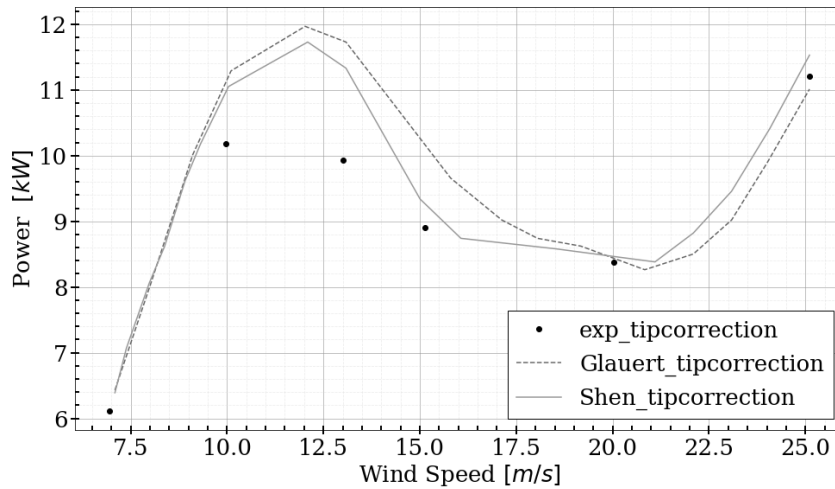


**Figure 2.3:** Results of the improved tip loss correction compared to the Glauert method by Shen et al. [2005]

wing, the effect of the trailing vortex is not included. Glauert [1935] proposes the first correction for the tip of the blade, however, the tip loss was assumed to only affect the induced velocity and not the mass flux. Shen et al. [2005] propose an improved correction model for the tip loss. The model by Shen et al. [2005] corrects for this mass flux error near the tip. Moreover, the model decreases the overestimation of the classical tip loss correction, of which the result can be found in figure 2.3. The figure demonstrates an improvement following experimental data, except for the higher ranges of wind speed. For these higher ranges the correction by Glauert [1935] is still on par with Shen et al. [2005].

Another source of error for the BEM model is the flow in the radial direction. Micallef et al. [2013] suggest a 3D potential flow model in which these effects may be modeled, also in yaw. DIPC can be seen as periodically yawing the flow when looking downstream of the wind turbine. Making the correction by Micallef et al. [2013] is potentially interesting for the BEM of DIPC.

BEM can very easily be applied to any rotor, provided the airfoil polars are known. By using the airfoil polars, the need to model the boundary layer is circumvented. This is what makes BEM ideal for coupled simulations of rotor wake flows, such as performed by Malki et al. [2013]. Moreover, this suggests the method is a suited one to couple with the Ainslie wake model to keep the computational cost low for the entire simulation. Additionally, Siemens Gamesa<sup>1</sup> has an in-house BEM script that is available for this research effort.

<sup>1</sup>The company which employs supervisor Norbert Warncke and cooperated in this research

## 2.3 Numerical Methods

The previously discussed wake models require numerical methods to be implemented. This section presents the motivation and consideration behind the different numerical methods. By no means do the presented methods form a complete set representing all available methods for this flow case. The methods discussed have favorable properties related to a semi-infinite domain, particularly useful properties in cylindrical coordinate systems, or are common spectral element bases.

The consequences of the wake model choices and fundamental theory are discussed in section 2.3.1. Thereon, the focus shifts to the different methods starting with the Jacobi polynomials section 2.3.2. Section 2.3.3 goes into the Bessel functions' usefulness with respect to the cylindrical wake model. The last spectral method bases discussed are the Hermite functions in section 2.3.4 and the Laguerre functions in section 2.3.5 for their semi-infinite support. Finally, the necessary downstream discretization technique is described in section 2.3.6.

### 2.3.1 Domain Partitioning

Utilizing the provided BEM script to obtain the inflow condition has consequences for the domain. An actuator disk with a loading that varies only in the radial direction results in an axisymmetrical velocity profile, so that, the domain is taken to be axisymmetric.

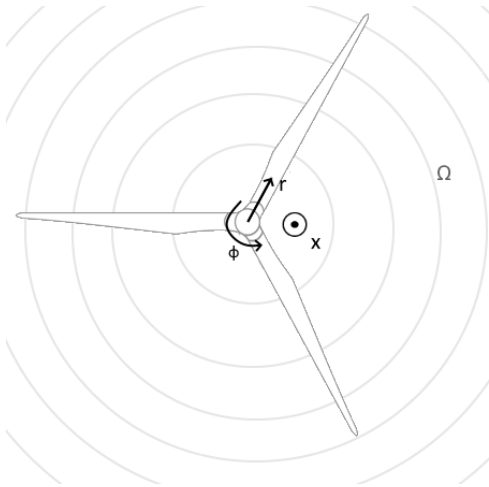
The x-dimension is defined as the downstream direction from the first wind turbine to the second wind turbine. The model will not account for the second wind turbine in any form, thus there is no difference between the analysis of a single wind turbine and a wind turbine in a park.

Partitioning the reference domain ( $\Omega$ ), or the domain of interest, in a simplicial set of grids  $B$ , provides discretization in the downstream direction. The number of grid elements in downstream directions will always be an integer value described with either  $q$  or  $n$ . These grids are not infinite, meaning they have boundaries defined as  $\partial B$ . The exterior boundary of the domain is denoted as  $\partial\Omega$ .

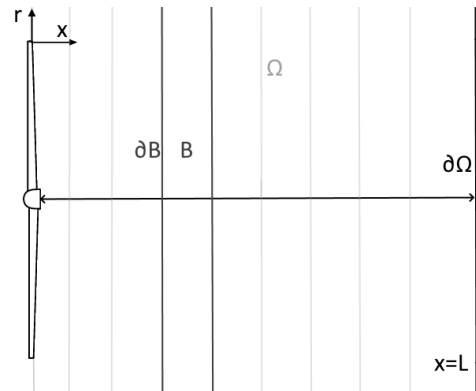
In the radial direction, one spectral element is applied with a semi-infinite domain. Functions in the spectral element are superimposed on top of each other and are not bound to cells, they are continuously differentiable.

The index of radial modes is described with  $k$  and  $q$ , whereas the accompanying projection will have the index  $m$  in the radial direction. The modes, in both dimensions, have an additional degree of freedom, which is the scaling constant.

A view from the back of the wind turbine is shown in figure 2.4a. It is important to note that the discretization in the radial direction is not bound by the circular elements.



(a) Circular domain downstream of the turbine. Adapted image from the work of Gözcü and Verelst [2020].



(b) Downstream discretization of the domain. Adapted image from the work of Schulte and Gauterin [2015].

Implementing bounded numerical domains typically comes with fixing aspects of the domain to match the set boundary conditions. Common practice dictates imposing the boundary conditions considerably far away from the domain to reduce the aphysical effects on the interested domain. Alternatively, a set of basis functions can be chosen that match the boundary conditions by definition.

Likewise, some boundary conditions could be gradually approached and do not need strict enforcement, the model may even benefit from allowing free expansion of the domain. This can be achieved by not having a limit on the domain at all, the semi-infinite domain reaching up to infinity. This can be achieved with spectral methods, which constitute the focus of this section.

Spectral methods were introduced with Fourier series as the basis functions. These Fourier bases spectral functions show amazing results for problems with periodic boundary conditions. When nonperiodic boundary conditions are present in the problem, the global convergence rate will be reduced to  $\mathcal{O}(N^{-1})$ , known as the Gibbs phenomenon formulated by Gottlieb and Orszag [1977].

Alternatively, orthogonal polynomials may be applied to non-periodic boundary conditions. Polynomials that are often used for this purpose are the Jacobi, the Legendre, the Chebyshev, and the Bessel polynomials. Rapid convergence may be achieved with the right selection of functions for the problem, as shown in figure 2.5. This phenomenon is known as spectral convergence.

Global connectivity comes with a sensitivity to local errors. When singularities occur somewhere in the domain, the error will directly affect the solution at all points. Similarly, the boundary conditions will affect the solution for the entire domain.

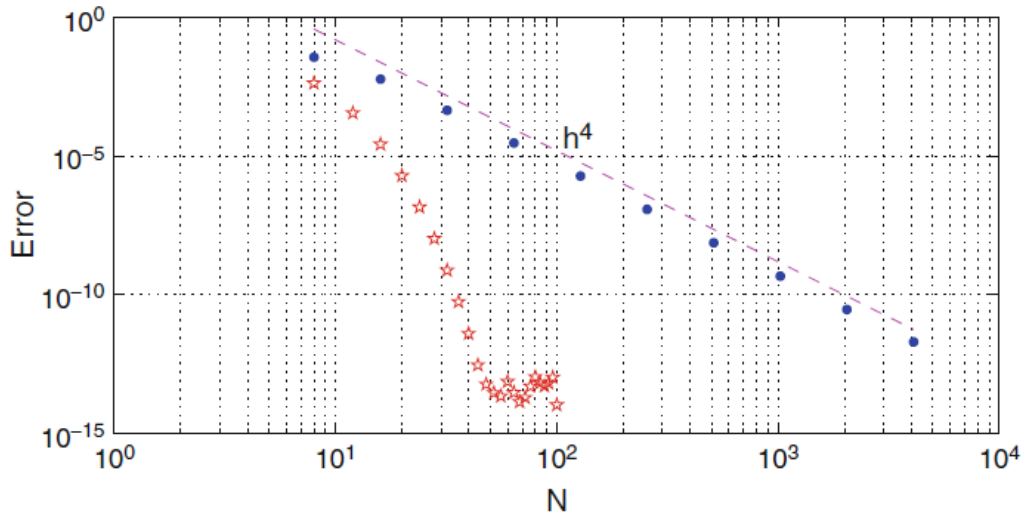


**Figure 2.5:** Convergence of 4th-order finite difference and Fourier-collocation differentiation processes (Shen et al. [2011]).

### Weak Formulation

The numerical discretization in both dimensions is based on a weak formulation. Due to the finite support of the basis functions in the axial dimension, a marching scheme is obtained that computes the flow field in successive steps downstream from an initial inflow condition.

Unlike what its name suggests, the weak formulation of the equations is a powerful tool in numerical methods to solve differential equations which may not have a 'strong' or a classical solution. Instead of requiring a stricter form of continuity, the continuity may be satisfied by what the definition of the integral entails. The result of the weak formulation is commonly known as the weak solution.

An exemplary weak formulation:

$$\int_{\Omega} L(u)b \, dV - \int_{\Omega} fb \, dV = 0 \quad (2.16)$$

Where  $L$  resembles a differential operator,  $b$  the projection function (also known as the test function),  $f$  a known function, and  $u$  the weak solution to the equation. This approach forms the basis of discretization in both dimensions.

Whether the integral covers a semi-infinite domain, such as for radial discretization, or a finite domain, such as in the downstream discretization, the fundamental approach remains the same.

The remainder of this section is dedicated to some of the typical spectral basis functions, specifically the ones that are potentially useful for the considered flow case, and a short review of their corresponding risks and benefits. This is not a complete collection of all available basis functions, but a collection based on semi-infinite support properties and benefits for the specific flow case.

### 2.3.2 Jacobi Basis

Jacobi polynomials,  $J_n^{\alpha,\beta}$ , can be employed as basis functions. Their usefulness lies in the orthogonality concerning the Jacobi weight function  $\omega^{\alpha,\beta}$ . The formulation of the Jacobi polynomials then becomes:

$$\int_{-1}^1 J_n^{\alpha,\beta} J_m^{\alpha,\beta} \omega^{\alpha,\beta}(x) dx = \gamma_n^{\alpha,\beta} \delta_{mn} \quad (2.17)$$

Where  $\omega = (1-x)^\alpha(1+x)^\beta$ . Multiple formulas satisfy this equation. Generally, these formulae concern their case-specific strengths. For instance, the Rodriguez formulation of the Jacobi polynomials results in either an even or an odd function depending on  $n$  in the sum. Jacobi polynomials could be a good fit for the nonperiodic boundary conditions in the direction of  $r$ .

Polynomials such as the Legendre and Chebyshev polynomials are the Jacobi class's most common spectral basis function in incompressible flow modeling, especially popular for spectral element methods (Karniadakis and Sherwin [2005]). However, these will not be taken up in this research due to the lack of semi-infinite support.

### 2.3.3 Bessel Functions

Arfken et al. [2013] describe Bessel functions' useful properties for physical problems. Bessel functions are, in principle, solutions of  $y(r)$  for Bessel's differential equation:

$$r^2 \frac{d^2 y}{dr^2} + r \frac{dy}{dr} + (r^2 - \alpha^2)y = 0 \quad (2.18)$$

The order of Bessel's function is described by  $\alpha$ . Bessel functions are good candidates for modeling the radial dimension. Bessel functions are often used in the modeling of cylindrical physical phenomena. The far-wake is likely to benefit the most from the Bessel basis functions. This is a consequence of the far-wake nearing a Gaussian distribution in velocity deficit. The opposite is then the case for the near-wake. Besides, poor near-wake modeling, the Bessel's function incorrectly approximates the effect of turbulent mixing. This downside may be minimal since the most interesting domain for this research is the far wake.

The specific Bessel functions of interest would be the Bessel functions of the first kind:

$$B_\alpha = \sum_{j=0}^{\infty} \frac{(-1)^j}{j! \Gamma(m + \alpha + 1)} \left(\frac{r}{2}\right)^{2m+\alpha} \quad (2.19)$$

Similarly to the Jacobi class polynomials, the Bessel functions of the first kind also have a beneficial orthogonality relation:

$$\int_0^\infty B_i(\alpha r) B_j(\alpha r) r dr = \frac{1}{2} (B_{i+1}(\alpha)) \delta_{ij} \quad (2.20)$$

Bessel functions of the first kind are a natural result for the Laplacian in a cylindrical coordinate system Kirkwood [2018]. This attribute of the Bessel function makes it a perfect choice for the modeling of the diffusion equation. Additionally, there exists a triple product integral approximation for Bessel functions, described by Auluck [2012], making the Bessel functions a serious candidate for the role of basis functions. Yet, the implementation of the Bessel functions will not be researched for the model, because the following alternatives have triple product integrals which may be directly computed.

### 2.3.4 Hermite Functions

The general notation of the Hermite function is described in equation (2.22), containing the Hermite “physicist’s” polynomials ( $H_n$ ), described in equation (2.21). What makes these functions applicable for modeling wakes, is their property of going to zero when approaching infinity. Additionally, the odd-order Hermite functions are zero at  $r = 0$ . For this reason, the odd-order Hermite functions form the basis of the radial velocity in the radial direction. Even-order Hermite functions are symmetric, which results in obeying the axisymmetric assumption. Committing the Hermite functions to the Ainslie equation results in the velocity formulations equation (2.23) and equation (2.24).

$$H_n(x) = (-1)^n e^{x^2} \frac{d^n}{dx^n} (e^{-x^2}) \quad (2.21)$$

$$\zeta_n(r) = (2^n n! \sqrt{\pi})^{\frac{1}{2}} e^{-\frac{r}{2}} H_n(r) \quad (2.22)$$

$$U = U_\infty - \sum_{k=0}^{2N_r-2} \zeta_{2k} \left[ \frac{x - x_l}{x_r - x_l} u_{kr} - \frac{x_r - x}{x_r - x_l} u_{kl} \right] \quad (2.23)$$

$$V = \sum_{k=0}^{2N_r-1} \zeta_{2k+1} \left[ \frac{x - x_l}{x_r - x_l} v_{kr} - \frac{x_r - x}{x_r - x_l} v_{kl} \right] \quad (2.24)$$

The explicit formulations of Hermite functions allow for integrals that are not directly solvable, to become explicitly computed:

$$H_{2n}(r) = (2n)! \sum_{l=0}^n \frac{(-1)^{n-l}}{(2l)!(n-l)!} (2r)^{2l} \quad (2.25)$$

$$H_{2n+1}(r) = (2n+1)! \sum_{l=0}^n \frac{(-1)^{n-l}}{(2l+1)!(n-l)!} (2r)^{2l+1} \quad (2.26)$$

Generally, the equations will lead to seven distinct integrals. The first three will be a product of two Hermite functions and the variable  $r$ . The latter four are products of three Hermite functions and a variable  $r$ . For the derivation of the expressions, the explicit even, in equation (2.25), and odd, in (equation (2.26)), formulations of the Hermite functions are used. Moreover, equation (2.27) is employed to write the entire integral in a series expansion. The first case covered is that of the integral of two even-order Hermite functions and  $r$ :

$$r^n e^{-r^2} = \frac{1}{2} \Gamma\left(\frac{n+1}{2}\right) \quad (2.27)$$

$$\begin{aligned} \int_0^\infty \zeta_{2k} \zeta_{2y} r \, dr &= (2k)! \sum_{l=0}^k \frac{(-1)^{n-l}}{(2l)!(n-l)!} (2r)^{2l} \\ &\quad (2y)! \sum_{l'=0}^y \frac{(-1)^{y-l'}}{(2l')!(y-l')!} (2r)^{2l'} r e^{-r^2} \\ \int_0^\infty \zeta_{2k} \zeta_{2y} r \, dr &= (2k)! (2y)! \sum_{l=0}^k \sum_{l'=0}^y \frac{(-1)^{n+y-l-l'}}{(2l)!(n-l)!(2l')!(y-l')!} (2)^{2l+2l'} r^{2l+2l'+1} e^{-r^2} \end{aligned} \quad (2.28)$$

The following relation helps simplify the equations to a useful format.

$$r^{2l+2l'+1} e^{-r^2} = \frac{1}{2} \Gamma(l+l'+1) \quad (2.29)$$

Leading to expressions that can be simplified to an explicit formulation equivalent.

$$\int_0^\infty \zeta_{2k} \zeta_{2y} r \, dr = \sum_{l=0}^k \sum_{l'=0}^y \frac{(-1)^{n+y-l-l'} (2)^{2l+2l'} (2k)! (2y)!}{(2l)! (n-l)! (2l')! (y-l')!} \frac{1}{2} \Gamma(l+l'+1) \quad (2.30)$$

This series can be further simplified by employing Wolfram, which leads to a general expression for the integral:

$$\frac{4^{l-1} (2l-1) (-1)^{k+y+1} (2k+2y+1) \Gamma(2k+1) \Gamma(y-\frac{1}{2})}{\sqrt{\pi} (2k-2y-1) (2k-2y+1) \Gamma(k+1)} \quad (2.31)$$

Not all integrals give a useful relation. The ones that do are:  $\int_0^\infty \zeta_{2k} \zeta_{2y}$ ,  $\int_0^\infty \zeta_{2k} \zeta_{2y+1}$  and  $\int_0^\infty \zeta_{2k+1} \zeta_{2y+1}$ , result in the general expressions:

$$\int_0^\infty \zeta_{2k} \zeta_{2y+1} \, dr = \frac{(-1)^{k+l+1} 2^{2k+2l+1} \Gamma(k+\frac{1}{2}) \Gamma(k+\frac{3}{2})}{\pi (2k-2l-1)} \quad (2.32)$$

$$\int_0^\infty \zeta_{2k} \zeta_{2y} \, dr = \sum_{l=0}^k \sum_{l'=0}^y \frac{(-1)^{n+m-l-l'} (2n)! (2m)! 2^{2l+2l'-1}}{(2l)! (k-l)! (2l')! (y-l')!} \Gamma(k+y+\frac{1}{2}) = \Phi(k) \quad (2.33)$$

$$\int_0^\infty \zeta_{2k+1} \zeta_{2y+1} = \sum_{l=0}^k \sum_{l'=0}^y \frac{(-1)^{n+m-l-l'} (2n+1)! (2m+1)! 2^{2l+2l'+1}}{(2l+1)! (k-l)! (2l'+1)! (y-l')!} \Gamma(k+y+\frac{3}{2}) = \Phi(k) \quad (2.34)$$

$\Phi$  is the Euler totient function. The interesting part of these outcomes is that the integrals only have an outcome when the even orders are the same or when the odd orders are the same. The integration is not as consistent when the integral contains the product of an even-order and an odd-order Hermite function.

Hermite functions have been taken up in the research as potential basis functions, however, the lack of an applicable orthogonality relation has obstructed the development of a Hermite-based model. With a direct relation to Laguerre polynomials, described by equation (2.35) and equation (2.36), transforming the Hermite-basis to Laguerre-basis where applicable was considered. Doing so will not yield Laguerre expressions that can be easily arranged to be solved. This motivated the research into Laguerre basis functions instead, which will be worked out in the next section.

$$H_{2n}(r) = (-1)^n 2^{2n} n! L_n^{-1/2}(r^2) \quad (2.35)$$

$$H_{2n+1}(r) = (-1)^n 2^{2n+1} n! r L_n^{1/2}(r^2) \quad (2.36)$$

### 2.3.5 Laguerre Functions

The Laguerre-Gaussian weighted functions, from hereon referred to as Laguerre functions, are the choice for the basis functions in the radial direction. Laguerre polynomials are the solutions to Laguerre's equation (Shen et al. [2011]):

$$r f'' + (\alpha + 1 - r) f' + n y = 0 \quad (2.37)$$

Laguerre functions are a product of a Laguerre polynomial (equation (2.38)) (Shen et al. [2011]) and a Gaussian  $e^{-\frac{r^2}{2}}$ . What makes Laguerre functions, specifically, such a good fit to the domain, is their orthogonality relation defined for Laguerre polynomials, shown in equation (2.40) (Shen et al. [2011]). This Laguerre function's orthogonality property keeps the resulting system of equations sparse.

$$L_k^{(\alpha)}(r) = \frac{e^r r^{-\alpha}}{k!} \frac{d^k}{dr^k} (e^{-r} r^{k+\alpha}) \quad (2.38)$$

$$\psi_k(r) = e^{-\frac{r^2}{2}} L_k(r^2) \quad (2.39)$$

$$\int_0^\infty r^\alpha e^{-r} L_k^{(\alpha)}(r) L_m^{(\alpha)}(r) = \frac{\Gamma(k + \alpha + 1)}{k!} \delta_{k,m} \quad (2.40)$$

Where  $\Gamma$  is the gamma-function ( $\Gamma = (k - 1)!$ ) and  $\alpha$  is the same  $\alpha$  as in equation (2.37).

By taking the Laguerre polynomials as a function of  $r^2$  instead of  $r$ , a more applicable set of functions is found for the radial direction, formulated in equation (2.41). Thus, generating the velocity expression of equation (2.42).

$$\psi_k(r) = L_k(r^2) e^{-\frac{r^2}{2}} \quad (2.41)$$

$$U = U_\infty - \sum_{k=0}^{N_r} \psi_k(r) \left[ \frac{x - x_l}{x_r - x_l} u_{kr} + \frac{x_r - x}{x_r - x_l} u_{kl} \right] \quad (2.42)$$

The accompanying projection in line with the Ritz-Galerkin method:

$$b_m(x, r) = \psi_m(r) \frac{x - x_l}{x_r - x_l} \quad (2.43)$$

Substituting 7.12a into 7.12b from the work by Shen et al. [2011]:

$$L_k^\alpha(r) = \underbrace{\frac{d}{dr} L_k^\alpha(r)}_{-L_{k-1}^{\alpha+1}(r)} - \underbrace{\frac{d}{dr} L_{k+1}^\alpha(r)}_{+L_k^{\alpha+1}(r)}$$

$$L_k^\alpha(r) = L_k^{\alpha+1}(r) - L_{k-1}^{\alpha+1}(r) \quad (2.44)$$

The derivatives of the Laguerre functions are described by the identity (2.45), computed directly from the derivative relation (Shen et al. [2011]). A recurrence relation can be applied to arrive at a sum notation of the derivative (2.46), which in turn may be expressed containing Laguerre functions (2.47).

$$\psi_k'(r) = \frac{d}{dr} \left( L_k(r^2) e^{-r^2/2} \right)$$

$$\psi_k'(r) = -r \left( L_k(r^2) + 2L_{k-1}^1(r^2) \right) e^{-r^2/2} \quad (2.45)$$

or,

$$\psi_k'(r) = -r \left( L_k(r^2) + 2 \sum_{i=0}^{k-1} L_i(r^2) \right) e^{-r^2/2} \quad (2.46)$$

$$\psi_k'(r) = -r \left( \psi_k(r^2) + 2 \sum_{i=0}^{k-1} \psi_i(r^2) \right) \quad (2.47)$$

The method of solving for the equation comes down to substituting  $r^2$  for  $z$  to allow for direct application of the orthogonality relation.

$$r^2 = z \quad (2.48)$$

$$2r dr = dz \quad (2.49)$$

This transformation can be used to transform an integral product of two Laguerre functions.

$$\int_0^\infty L_k(r^2) L_m(r^2) e^{-r^2} r dr = \frac{1}{2} \int_0^\infty L_k(z) L_m(z) e^{-z} dz$$

$$= \frac{1}{2} \int_0^\infty \psi_k(z) \psi_m(z) dz \quad (2.50)$$

This is what makes the adjusted Laguerre functions very well applicable to the cylindrical coordinate system. For a more typical implementation of the Laguerre functions, more recurrence relations would be required to work-out the  $r$ -scalar.

Moreover, an explicit formulation (equation (2.52)) of the triple-product integral exists for Laguerre functions (Gillis and Shimshoni [1962]). The explicit formulation of triple product integrals omits the need for approximations of the integrals, providing another motivation for the Laguerre functions.

$$C_{k,q,m} = \sum_{k,q,m=0}^{N_r} \int_0^{\infty} \psi_k(r)\psi_q\psi_m dr \quad (2.51)$$

$$C_{k,q,m} = \frac{2}{3} \sum_{\epsilon,\beta,\gamma=0}^{k,q,m} \left(-\frac{2}{3}\right)^{k+q+m} \binom{k}{\epsilon} \binom{q}{\beta} \binom{m}{\gamma} \frac{(\epsilon + \beta + \gamma)!}{\epsilon! \beta! \gamma!} \quad (2.52)$$

Implementation of this explicit expression requires careful consideration. Most scripting tools will not return an accurate result for somewhat high values of  $k, l$ , and  $m$ . This numerical error may be reduced by rewriting the expression in logarithmic form:

$$\ln \left( \binom{k}{\alpha} \right) = \ln(k!) - \ln(\alpha!) - \ln((k - \alpha)!) \quad (2.53)$$

The logarithmic expression of the Laguerre functions with as highest orders  $\approx 8$  still has a satisfactory error. For higher orders, the symmetry of the expression disappears, indicating an increase in error. Handling this error requires high-precision methods. The Python module `mpmath` goes up to orders of approximately 13 before resulting in an error that cannot be accepted. A desktop computer took a bit over 4 hrs to tabulate the data up to an order of 31. Even though symmetry checks of the expression showed residuals in the range of 0.1 – 40% for orders around 14, the expression has been tabulated up to an order of 31. Appendix A from Gillis and Shimshoni [1962] provides means to check the validity up to a 10th-order integral. Within this range, the values have been checked to see whether they correspond to the tabulated values. Besides the obvious limitation of precision, the tabulated expressions from Gillis and Shimshoni [1962] only have a precision of  $10^8$ . Verifying the outcomes beyond the provided tabulated data is outside the scope of this research.

All three functions come with their advantages and disadvantages. The aforementioned Bessel functions do not come with a simple solution for the triple product integral. The Hermite functions may be expressed in terms of Laguerre functions, meaning with some arithmetic effort some cases the expressions can be completely expressed

in the other, however, the benefits of the Laguerre functions outweigh those of the Hermite, namely, the explicit triple product integral expression and the orthogonality relation for the axisymmetric semi-infinite domain.

Furthermore, Shen et al. [2011] describe Gauss-Laguerre quadratures, which could be explored as an alternative to the explicit triple product integral. This option is not explored in this research, instead, the equations will be modeled with Laguerre functions as the basis functions in the radial direction and the triple product integrals approximated by equation (2.52).

### 2.3.6 Marching Scheme

For the downstream discretization, a Finite Element marching scheme is employed. This will be a continuous Ritz-Galerkin implementation. Continuity follows from the fact that the basis functions form a continuous basis between the grid elements.

The basis functions discussed in this section are piecewise linear, thus can be differentiated once, and are a first-order Sobolev space. A schematic diagram of these basis functions is shown in figure 2.6. For its first derivative, the functions are piecewise constant. The equations belonging to the piecewise linear function are provided in equation (2.54). For an element purely discretized in the axial direction, the support is defined by equation (2.55).

$$x_r = \frac{x - x_l}{x_r - x_l}, \quad x_l = \frac{x - x_l}{x_r - x_l} \quad (2.54)$$

$$b(x) = \frac{x - x_l}{x_r - x_l} \quad (2.55)$$

These piecewise linear basis functions are a simplicial set, defined by the first order Hilbert space, such that:

$$h_k := \{h_k \in H^1(\mathcal{T})\} \quad (2.56)$$

The  $H^1$  notation indicates a Sobolev space. The general Sobolev space  $H^k$  can be used to describe a function, such that:

$$H^k = \left\{ f : \int_{\Omega} f^2 + \|\nabla^1 f\|^2 + \|\nabla^2 f\|^2 \dots + \|\nabla^k f\|^2 \right\} < \infty \quad (2.57)$$

An example of a function that would not satisfy the  $H^1$ -space is a step-function. The discontinuity blows up the derivative to infinity. Hence, a step-function does not satisfy the requirement to be  $H^1$ -space. This definition is used to indicate the level of continuity for the respective functions over the domain. Considering the piecewise linear functions

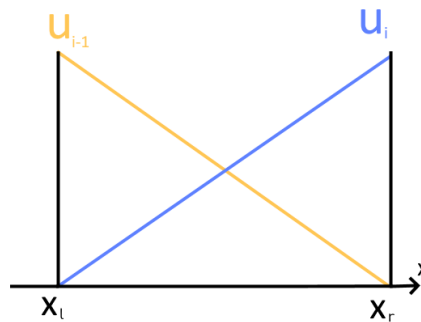


**Figure 2.6:** Linear basis function used for finite element method in axial direction

in figure 2.6 become piecewise constant functions when differentiated once, the second derivative goes to infinity between the transitions from one coefficient constant to the other.

Piecewise linear functions come with the benefit of having simple integrals. The derivative of a linear function immediately loses all dependency on  $x$ . This means that not just an integral can be computed straightforwardly, also, the derivative can be computed directly. This simplicity exhibits not only positives but the continuity of the derivative terms also will not be upheld, accordingly, causing discontinuities between the left and right sides.

Marching schemes consist of a right side and a left side of the respective elements. This is indicated by the subscripts l (left) and r (right).

Regularly, CFD can not be performed with a marching scheme. By neglecting the pressure term, a parabolic approach may be applied to the equations. This fixes the flow of information in the downstream direction, consequently, the axial velocity can never become negative, effectively, constraining the approach to advection-dominated flow cases.

Arguably, this may be an unsatisfactory level of continuity and information flow for fluid simulations. Radial discretization is the focus of this study, thus, lowering continuity to meet the time constraint of the research is considered acceptable.

## 2.4 Conclusion

In this chapter, the application of the Ainslie wake model with a BEM to model the flow case is suggested to be the best choice. There are issues of concern regarding the asymmetric nature of DIPC combined with Ainslie's wake model. A few alterations to the model are suggested, which may bring the model up to satisfactory performance. By

applying a BEM to model the turbine, the most complicated aspect of the wind turbine wake modeling is removed from the model. Potentially, resulting in a model with low computational cost.

The simulation is supported by Laguerre functions in the radial direction, owing to the useful orthogonality relation and the explicit triple product integral. There are concerns regarding the implementation of the explicit triple product integral, especially, regarding the consequences of the limited amount of available radial modes. In the downstream direction, the simulation will be completed with piecewise linear basis functions.

# Chapter 3

## Two-Dimensional Modeling

This chapter concerns itself with the numerical implementation required to model the Ainslie equation. The methods used to model the equation are Laguerre functions for the radial dimension and a FE marching scheme in the axial dimension.

In this chapter, section 3.1 is worked out for the respective discretization and in section 3.2 the momentum equation is worked out.

### 3.1 Mass Continuity

The time-averaged mass continuity equation (3.1) is the first equation to be solved.

$$\nabla \cdot \begin{pmatrix} U \\ V \\ W \end{pmatrix} = 0 \quad (3.1)$$

Taking the divergence in cylindrical coordinates and realizing the basis functions are independent of azimuthal angle, leads to equation (3.2).

$$\nabla \cdot \begin{pmatrix} U(x, r) \\ V(x, r) \\ W(x, r) \end{pmatrix} = \frac{\partial U(x, r)}{\partial x} + \frac{1}{r} \frac{\partial}{\partial r} (rV(x, r)) + \underbrace{\frac{1}{r} \frac{\partial W}{\partial \theta}}_{\frac{\partial W}{\partial \theta} = 0} = 0 \quad (3.2)$$

#### 3.1.1 Natural Radial Basis Functions

Before proceeding with solving the equation, the radial velocity must be expressed. Due to the simplicity of the mass equation, a natural expression for the radial velocity can

be derived from the mass equation<sup>2</sup>. Employing a substitution in place of  $V$  with  $\frac{\partial U}{\partial x}$  yields a few additional benefits. First of all, being able to further reduce the number of equations required for this system, leads to lower computational costs. Secondly, the substitution results in pointwise satisfaction of the mass equation. This means that the conservation is no longer fulfilled in a weak sense as described in section 2.3.1. As with most choices in numerical analysis, there is also a downside, in this case, that of reduction of the order for  $V$  in the axial direction.

In this implementation of the equation, the substitution is emitted, however, the worked-out approach is included in appendix A. Do consider with such an implementation that one loses the advantages of the weak formulation for  $V$ . Additionally,  $V$  in this case becomes become a step function because it is directly defined by the derivative of  $U$ .

Deriving the discretization for the basis function of  $V$  may be done by taking the mass equation and putting the terms on opposite sides, as such:

$$\begin{aligned} \frac{1}{r} \frac{\partial}{\partial r} (rV(x, r)) &= - \frac{\partial U(x, r)}{\partial x} \\ rV(x, r) &= - \int_0^r \rho \frac{\partial U(x, \rho)}{\partial x} d\rho \end{aligned} \quad (3.3)$$

The next step is to include the radial basis function for  $\frac{\partial U(x, r)}{\partial x}$ .

$$rV(x, r) = - \sum_{k=0}^{N_r} \frac{\partial U_k(x)}{\partial x} \int_0^r \rho \psi_k(\rho) d\rho \quad (3.4)$$

The focus for the next part lies on  $\int_0^r \rho \psi_k(\rho) d\rho$ . By taking the integral of the derivative (equation (2.47)) of the Laguerre function, a substitution of expressions can be prepared.

$$\begin{aligned} \int_0^r \frac{\partial}{\partial \rho} \psi_k(\rho) d\rho &= - \int_0^r \psi_k(\rho) \rho d\rho - 2 \sum_{i=0}^{k-1} \int_0^r \psi_i(\rho) \rho d\rho \\ \psi(r) - \underbrace{\psi(0)}_{=1} &= - \underbrace{\int_0^r \psi_k(\rho) \rho d\rho}_{I_k(r)} - 2 \sum_{i=0}^{k-1} \underbrace{\int_0^r \psi_i(\rho) \rho d\rho}_{I_i(r)} \end{aligned} \quad (3.5)$$

With a minor rearrangement arriving at:

---

<sup>2</sup>Provided by supervisor N. Warncke.

$$I_k(r) = 1 - \psi_k(r) - 2 \sum_{i=0}^{k-1} I_i(r) \quad (3.6)$$

This is a recursive relation that runs up to the Laguerre function of order 0. Plugging this back into the expression for V provides the used radial expression. The result of this proof is:

$$rV(x, r) = - \sum_{k=0}^{N_r} 1 - \psi_k(r) - 2 \sum_{i=0}^{k-1} I_i(r) \frac{\partial U_k(x)}{\partial x} \quad (3.7)$$

Leading to the natural choice for  $V(x, r)$  as:

$$V = \sum_{k=0}^{N_r} \frac{1}{r} (1 - \psi_k(r)) \left[ \frac{x - x_l}{x_r - x_l} v_{kr} + \frac{x_r - x}{x_r - x_l} v_{kl} \right] \quad (3.8)$$

Do note, that this expression for V supports the axisymmetric boundary condition and the condition for V going to zero for  $r \rightarrow \infty$ . At  $r=0$ , the exponential part of the Laguerre function ( $\psi$ ) tends faster to 1 than  $\frac{1}{r}$  tends to  $\infty$ , thus,

$$\lim_{r \rightarrow 0} \frac{1}{r} (1 - \psi_k(r)) = 0 \quad (3.9)$$

### 3.1.2 The System of Mass Continuity

Applying the Galerkin projection and the weak formulation to the mass equation (3.2) results in equation (3.10).

$$\sum_{k=0}^{N_r} \iint_{\Omega} b_{m,y} \frac{\partial U(x, r)}{\partial x} r \, dr \, dx + \sum_{k=0}^{N_r} \iint_{\Omega} b_{m,y} \frac{1}{r} \frac{\partial}{\partial r} (rV(x, r)) r \, dr \, dx = 0 \quad (3.10)$$

By applying the notation for the downstream discretization of equation (B.13), the first term of equation (3.2) can be worked out directly:

$$\begin{aligned}
\iint_{\Omega} b(x, r) \frac{\partial U}{\partial x} r \, dr \, dx &= - \iint_{\Omega} \sum_{k=0}^{N_r} \psi_k(r) \psi_m(r) \frac{x - x_l}{x_r - x_l} \\
&\quad \left[ \frac{1}{x_r - x_l} u_{kr} - \frac{1}{x_r - x_l} u_{kl} \right] r \, dr \, dx \quad (3.11) \\
&= - \frac{1}{2} \int_{x_l}^{x_r} \frac{x - x_l}{x_r - x_l} \, dx \sum_{k=0}^{N_r} \int_0^{\infty} \psi_k(z) \psi_m(z) e^{-z} \, dz \left[ \frac{1}{x_r - x_l} u_{kr} - \frac{1}{x_r - x_l} u_{kl} \right] \\
&\quad \iint_{\Omega} b_m \frac{\partial U}{\partial x} r \, dr \, dx = - \frac{1}{2} \sum_{k=0}^{N_r} \delta_{k,m} [u_{kr} - u_{kl}] \quad (3.12)
\end{aligned}$$

The same expression in matrix notation:

$$\iint_{\Omega} b_m \frac{\partial U}{\partial x} r \, dr \, dx = - \frac{1}{2} \mathbb{I}(\mathbf{u}_r - \mathbf{u}_l) \quad (3.13)$$

Next is the radial term of the mass equation, which reads, with the expression for the radial velocity:

$$\begin{aligned}
\iint_{\Omega} b(x, r) \frac{1}{r} \frac{\partial(rV)}{\partial r} r \, dr \, dx &= \iint_{\Omega} \sum_{k=0}^{N_r} \frac{x - x_l}{x_r - x_l} \left[ \frac{x - x_l}{x_r - x_l} v_{kr} + \frac{x - x_l}{x_r - x_l} v_{kl} \right] \\
&\quad \psi'_k(r) \psi_m(r) r \, dr \, dx \\
&= \int_{x_l}^{x_r} \sum_k^N \frac{x - x_l}{x_r - x_l} \left[ \frac{x - x_l}{x_r - x_l} v_{kr} + \frac{x - x_l}{x_r - x_l} v_{kl} \right] \\
&\quad \int_0^{\infty} \left( \psi_k(r) + 2 \sum_{i=0}^{k-1} \psi_i(r) \right) \psi_m r \, dr
\end{aligned}$$

The marching scheme can be straightforwardly integrated:

$$\int_{x_l}^{x_r} \sum_{k=0}^N \frac{x - x_l}{x_r - x_l} \left[ \frac{x - x_l}{x_r - x_l} v_{kr} + \frac{x - x_l}{x_r - x_l} v_{kl} \right] = \Delta x \sum_{k=0}^N \left[ \frac{1}{3} v_{kr} + \frac{1}{6} v_{kl} \right] \quad (3.14)$$

Transforming the r-domain to the z-domain as described by equation (2.48) and applying the orthogonality relation to the Laguerre functions, establishes the final expression for the radial modes:

$$\sum_{k=0}^N \int_0^{\infty} \left( \psi_k(r) + 2 \sum_{i=0}^{k-1} \psi_i(r) \right) \psi_m r dr = \sum_{k=0}^N \left( \delta_{k,m} + 2 \sum_{i=0}^{k-1} \delta_{i,m} \right) v_k \quad (3.15)$$

Combining the two terms and writing the equation in a matrix expression:

$$\Delta x \sum_{k=0}^N (\delta_{k,m} + 2 \sum_{i=0}^{k-1} \delta_{i,m}) \left[ \frac{1}{3} v_{kr} + \frac{1}{6} v_{kl} \right] = \Delta x \begin{bmatrix} 1 & 2 & \dots & 2 & 2 \\ 0 & 1 & & & \\ \vdots & & \ddots & & \vdots \\ & & & 1 & 2 \\ 0 & \dots & 0 & 0 & 1 \end{bmatrix} \left[ \frac{1}{3} \mathbf{v}_r + \frac{1}{6} \mathbf{v}_l \right] \quad (3.16)$$

## 3.2 Momentum Equation

This section details the setup of the matrices belonging to the momentum equation described in equation (2.13), including the implementation of the numerical analysis for both the diffusion and the nonlinear terms in the momentum equation.

### 3.2.1 Diffusion Term

In the work by Ainslie [1988], the mean quantities in the axial direction may be neglected, because in his approach the wake starts a few diameters downstream of the wind turbine. This model starts immediately behind the wind turbine, in effect, the two-dimensional diffusion equation is employed:

$$\iint_{\Omega} \nu_T \nabla \cdot \left( \nabla \begin{bmatrix} U(x, r) \\ V(x, r) \end{bmatrix} \right) \quad (3.17)$$

The viscosity in the diffusion equation is treated as a piecewise constant scalar quantity determined by an empirical fit, defined by equation (2.15). Its value is approximated by taking the average of the two elements:

$$\bar{\nu}_T \approx \frac{\nu_T(x_r) + \nu_T(x_l)}{2} \quad (3.18)$$

The simplicity of the equation may be enhanced by approaching the equations differently. By administering the product rule, a simpler expression can be arrived upon. Do note that in example equation (3.19)  $g$  is a scalar, similarly, as for the projection:  $b_m$ .

$$\nabla \cdot (gf) = \nabla g f + g \nabla \cdot f \quad (3.19)$$

The diffusion term does not contain  $\nabla \cdot (fg)$ , but  $g \nabla \cdot f$ . Thus, the rearranged application for the diffusion term becomes:

$$\begin{aligned} \iint_{\Omega} b_m(x, r) \nabla \cdot (\bar{\nu}_T \nabla U(x, r)) \, dV &= \iint_{\Omega} \nabla \cdot (b_m(x, r) \bar{\nu}_T \nabla U(x, r)) \, dV \\ &\quad - \iint_{\Omega} (\nabla b_m(x, r)) \cdot (\bar{\nu}_T \nabla U(x, r)) \, dV \end{aligned}$$

$\iint_{\Omega} \nabla \cdot (b_m(x, r) \bar{\nu}_T \nabla U(x, r)) \, dV$  may be rewritten by means of the divergence theorem (3.20) (Anderson [2017]). The application of the divergence theorem yields equation (3.21).

$$\iint_{\Omega} \nabla \cdot f \, dV = \oiint_{\partial\Omega} \vec{n} \cdot f \, dA \quad (3.20)$$

$$\iint_{\Omega} \nabla \cdot (b_m(x, r) \bar{\nu}_T \nabla U(x, r)) \, dV = \oiint_{\partial\Omega} b_m(x, r) \bar{\nu}_T (\vec{n} \cdot \nabla U(x, r)) \, dA \quad (3.21)$$

The result of the divergence theorem is the surface integral at the boundaries of the domain. In the case of the cylindrical domain, this yields four distinguishable boundaries.  $\partial\Omega_1$  at  $r \rightarrow \infty$ ,  $\partial\Omega_2$  at  $r = 0$ ,  $\partial\Omega_3$  at  $x = 0$ , and  $\partial\Omega_4$  at  $x = L$ .

The first surface integral over  $\partial\Omega_1$  will always be zero. This follows from the chosen basis function approaching zero for  $r \rightarrow \infty$ :

$$\oiint_{\partial\Omega_1} \lim_{r \rightarrow \infty} \underbrace{(b_m(x, r) \bar{\nu}_T (\vec{n} \cdot \nabla U(x, r)))}_{=0} \, dA \quad (3.22)$$

$\partial\Omega_2$  may be omitted too. This follows from the choice of basis function. Laguerre function's first derivative is zero at  $r=0$ , meaning  $\frac{\partial U(x,0)}{\partial r} = 0$ , thus the integral reduces to:

$$\oiint_{\partial\Omega_2} (b_m(x, 0) \bar{\nu}_T \underbrace{\left( \begin{bmatrix} 0 \\ -1 \end{bmatrix} \cdot \begin{bmatrix} \frac{\partial U(x,0)}{\partial x} \\ \frac{\partial U(x,0)}{\partial r} \end{bmatrix} \right)}_{=0}) \, dA \quad (3.23)$$

The other two boundaries to be considered are at  $x = x_l$  and  $x = x_r$ , which will lead to the first nonzero integrals. Firstly, the boundary integral at  $x = x_l$  results in zero, following from  $b(0, r) = 0$ , leaving the integral at the boundary  $x = x_r$ .

The projection at the boundary  $x = x_r$  does not tend to zero, nor do the basis functions in the marching scheme. The integral thus becomes:

$$\begin{aligned} \oint_{\partial\Omega_4} b_m(x_r, r) \bar{\nu}_T (\vec{n} \cdot \nabla U(x_r, r)) \, dA &= \iint_{\partial\Omega_4} b_m(x_r, r) \bar{\nu}_T \left( \begin{bmatrix} 1 \\ 0 \end{bmatrix} \cdot \begin{bmatrix} \partial U(x_r, r)/\partial x \\ \partial U(x_r, r)/\partial r \end{bmatrix} \right) \, dA \\ &= \oint_{\partial\Omega_4} b_m(x_r, r) \bar{\nu}_T \frac{\partial U(x_r, r)}{\partial x} \, dA \end{aligned} \quad (3.24)$$

Working out the expression, yields:

$$\begin{aligned} \oint_{\partial\Omega_4} b_m(x_r, r) \bar{\nu}_T \frac{\partial U(x_r, r)}{\partial x} \, dA &= \int_0^\infty \sum_{k=0}^{N_r} \psi_m(r) \psi_k(r) \left[ \frac{1}{x_r - x_l} u_{kr} - \frac{1}{x_r - x_l} u_{kl} \right] r \, dr \\ \oint_{\partial\Omega_4} b_m(x_r, r) \bar{\nu}_T \frac{\partial U(x_r, r)}{\partial x} \, dA &= \frac{1}{2} \sum_{k=0}^{N_r} \delta_{k,m} \frac{1}{\Delta x} [u_{kr} - u_{kl}] \end{aligned} \quad (3.25)$$

Or equivalently:

$$= \frac{\bar{\nu}_T}{2\Delta x} \mathbb{I}[\mathbf{u}_r - \mathbf{u}_l] \quad (3.26)$$

Next in the diffusion equation is the derivation with respect to the radial term.

$$\begin{aligned} -\bar{\nu}_T \iint_{\Omega} \frac{\partial b_m(x, r)}{\partial r} \frac{\partial U(x, r)}{\partial r} r \, dr \, dx &= \bar{\nu}_T \iint_{\Omega} \sum_{k,q=0}^{N_r} \frac{x - x_l}{x_r - x_l} \psi'_m(r) \\ &\quad \left( \frac{x - x_l}{x_r - x_l} u_{kr} + \frac{x_r - x}{x_r - x_l} u_{kl} \right) \psi'_k(r) r \, dr \, dx \\ &= \bar{\nu}_T \iint_{\Omega} \left( \frac{(x - x_l)^2}{(x_r - x_l)^2} u_{kr} + \frac{(x - x_l)(x_r - x)}{(x_r - x_l)^2} u_{kl} \right) \psi'_m(r) \psi'_k(r) r \, dr \, dx \end{aligned}$$

Integrating the expression with respect to  $x$  yields:

$$\sum_{k=0}^{N_r} \int_{x_l}^{x_r} \left( \frac{(x-x_l)^2}{(x_r-x_l)^2} u_{kr} + \frac{(x-x_l)(x_r-x)}{(x_r-x_l)^2} u_{kl} \right) dx = \sum_{k=0}^{N_r} \Delta x \left( \frac{1}{3} u_{kr} + \frac{1}{6} u_{kl} \right) \quad (3.27)$$

The radial integration is a more complicated matter. Picking the right recurrence relations simplifies things considerably. Starting from  $\int_0^\infty \psi'_m(r) \psi'_k(r) r dr$  and working-out the derivatives with equation (2.45) leads to the expression:

$$\int_0^\infty \psi'_m(r) \psi'_k(r) r dr = \int_0^\infty r^3 (L_k(r^2) + 2L_{k-1}^1(r^2))(L_m(r^2) + 2L_{m-1}^1(r^2)) e^{-r^2} dr \quad (3.28)$$

Realizing that the orthogonality relation (2.40) is also defined for Laguerre polynomials of  $\alpha > 0$ , changes the objective for solving this equation. Applying the recurrence relation (2.44) leads to all terms to be expressed in  $\alpha = 1$ , which, when the domain transformation (2.48) is applied, satisfies the orthogonality relation. The explanation expressed:

$$\begin{aligned} \int_0^\infty \psi'_m(r) \psi'_k(r) r dr &= \int_0^\infty r^3 (L_k(r^2) + 2L_{k-1}^1(r^2))(L_m(r^2) + 2L_{m-1}^1(r^2)) e^{-r^2} dr \\ &= \frac{1}{2} \int_0^\infty z (L_k^1(z) - L_{k-1}^1(z) + 2L_{k-1}^1(z))(L_m^1(z) - L_{m-1}^1(z) + 2L_{m-1}^1(z)) e^{-z} dz \\ &= \frac{1}{2} \int_0^\infty z (L_k^1(z) + L_{k-1}^1(z))(L_m^1(z) + L_{m-1}^1(z)) e^{-z} dz \end{aligned} \quad (3.29)$$

With the worked-out orthogonality relations, the integral can be described by equation (3.30). Substituting this expression back into the term derivative to r leads to equation (3.31), and its matrix form, equation (3.32).

$$\sum_{k=0}^{N_r} \int_0^\infty \psi'_m(r) \psi'_k(r) r^2 dr = \frac{1}{2} \sum_{k=0}^{N_r} (2k+1) \delta_{k,m} + k \delta_{k-1,m} + m \delta_{k,m-1} \quad (3.30)$$

$$= \frac{1}{2} \Delta x \sum_{k=0}^{N_r} ((2k+1) \delta_{k,m} + k \delta_{k-1,m} + m \delta_{k,m-1}) \left( \frac{1}{3} u_{kr} + \frac{1}{6} u_{kl} \right) \quad (3.31)$$

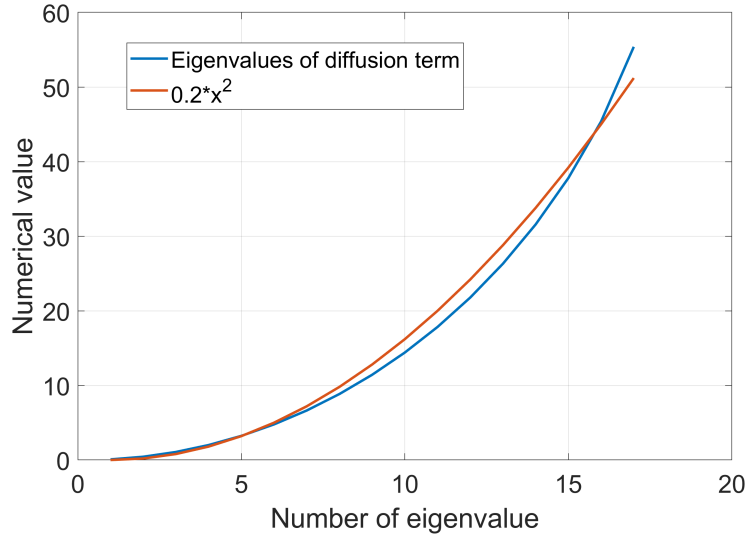


**Figure 3.1:** Comparison of the eigenvalues for the radial derivative diffusion term with respect to a scaled quadratic function. All elements adhere to being nonzero.

$$\begin{pmatrix}
 1 & 1 & & \dots & & & & \mathbf{0} \\
 1 & 3 & 2 & & & & & \\
 & 2 & 5 & 3 & & & & \\
 \vdots & & & \ddots & & & & \vdots \\
 & & & & N-3 & 2N-3 & N-2 & \\
 \mathbf{0} & & & & & N-2 & 2N-1 & N-1 \\
 & & & \dots & & 0 & N-1 & 2N+1
 \end{pmatrix} \quad (3.32)$$

The diffusion equation can be verified by comparing it with a similar discretization with Bessel equations (Kirkwood [2018]). The eigenvalues to the solution should adhere to a quadratic profile, and should all be nonzero, which is tested for and displayed in figure 3.1. The term of the diffusion equation containing the derivatives with respect to  $x$ ,

$$- \iint_{\Omega} \frac{\partial b_m(x, r)}{\partial x} \frac{\partial U(x, r)}{\partial x} dV \quad (3.33)$$

can be worked out more straightforwardly:

$$\begin{aligned}
- \iint_{\Omega} \frac{\partial b_m(x, r)}{\partial x} \frac{\partial U(x, r)}{\partial x} dV &= - \iint_{\Omega} \bar{\nu}_T \sum_{k,l=0}^{N_r} \frac{1}{x_r - x_l} \psi_m(r) \\
&\quad \left( \frac{1}{x_r - x_l} u_{kr} - \frac{1}{x_r - x_l} u_{kl} \right) \psi_k(r) r dr dx \\
&= - \bar{\nu}_T \int_{x_l}^{x_r} \sum_{k,l=0}^{N_r} \frac{1}{x_r - x_l} \left( \frac{1}{x_r - x_l} u_{kr} - \frac{1}{x_r - x_l} u_{kl} \right) dx \int_0^{\infty} \psi_m(r) \psi_k(r) r dr
\end{aligned}$$

Directly applying the domain transition and the orthogonality relation,

$$\int_0^{\infty} \psi_m(r) \psi_k(r) r dr = \frac{1}{2} \delta_{k,m} \quad (3.34)$$

and integrating with respect to  $x$

$$\int_{x_l}^{x_r} \frac{1}{x_r - x_l} \left( \frac{1}{x_r - x_l} u_{kr} - \frac{1}{x_r - x_l} u_{kl} \right) dx = \frac{1}{\Delta x} (u_{kr} - u_{kl}) \quad (3.35)$$

results in the final expression for the derivative with respect to  $x$  in the viscosity equation:

$$-\frac{1}{2\Delta x} \mathbb{I}(\mathbf{u}_r - \mathbf{u}_l) \quad (3.36)$$

### 3.2.2 Nonlinear Terms

With the diffusion term figured out, the nonlinear terms now follow. The final stages of writing out the nonlinear terms are approached differently than the differential equation. Instead of applying an orthogonality relation to simplify the integrals, the resulting integral must be approximated. Additionally, the resulting matrix will not be sparse. The first term;

$$\frac{\partial U(x, r)}{\partial x} U(x, r) \quad (3.37)$$

The term subjugated to the Galerkin projection and expressed in its weak formulation yields:

$$\iint_{\Omega} b(x, r) \frac{\partial U(x, r)}{\partial x} U(x, r) dV \quad (3.38)$$

Substituting the expressions for the velocity and rewriting is the next step to come to a final expression, the derivation of this expression reads:

$$\begin{aligned} \iint_{\Omega} b(x, r) \frac{\partial U(x, r)}{\partial x} U(x, r) dV &= \int_0^{\infty} \int_{x_l}^{x_r} \sum_{k,q=0}^{N_r} -\psi_m \frac{x-x_l}{x_r-x_l} \left[ \frac{1}{x_r-x_l} u_{kr} - \frac{1}{x_r-x_l} u_{kl} \right] \\ &\quad \psi_k(r) \left( U_{\infty} - \left[ \frac{x-x_l}{x_r-x_l} u_{rq} + \frac{x_r-x}{x_r-x_l} u_{ql} \right] \psi_l \right) r dx dr \\ &= \int_0^{\infty} \int_{x_l}^{x_r} \sum_{k,q=0}^{N_r} -U_{\infty} r \psi_m \psi_k \frac{x-x_l}{x_r-x_l} \left[ \frac{1}{x_r-x_l} u_{kr} - \frac{1}{x_r-x_l} u_{kl} \right] dx dr + \\ &+ \int_0^{\infty} \int_{x_l}^{x_r} \sum_{k,q=0}^{N_r} r \psi_m \psi_k \psi_q \frac{x-x_l}{x_r-x_l} \left[ \frac{1}{x_r-x_l} u_{kr} - \frac{1}{x_r-x_l} u_{kl} \right] \left[ \frac{x-x_l}{x_r-x_l} u_{qr} + \frac{x_r-x}{x_r-x_l} u_{ql} \right] dx dr \\ &= -U_{\infty} \sum_{k,q=0}^{N_r} \delta_{k,m} \left[ \frac{1}{2} u_{kr} - \frac{1}{2} u_{kl} \right] \\ &\quad + \frac{1}{2} \sum_{k,q=0}^{N_r} C_{k,q,m} \left[ \frac{1}{3} u_{kr} u_{qr} - \frac{1}{3} u_{kl} u_{qr} + \frac{1}{6} u_{kr} u_{ql} - \frac{1}{6} u_{kl} u_{ql} \right] \end{aligned}$$

From the final expression for  $U \frac{\partial U}{\partial x}$ , two distinct terms may be recognized; a linear term with the incoming velocity and a nonlinear term with the triple product integral. Expressing the first term in matrix notation yields:

$$-U_{\infty} \mathbb{I} \left( \frac{1}{2} \mathbf{u}_r - \frac{1}{2} \mathbf{u}_l \right) \quad (3.39)$$

For the second term the expression in matrix notation is more complicated. The most useful notation for the nonlinear terms is in the form of a vector. Each row of the vector represents a projection in  $m$  and contains the double sum for  $k$  and  $q$ . Solving nonlinear equations comes with certain requirements. The method that motivates the notation is described in section 3.2.3.

$$\begin{bmatrix} \sum_{k,q=0}^{N_r} C_{k,q,0} \left[ \frac{1}{3}u_{kr}u_{qr} - \frac{1}{3}u_{kr}u_{ql} + \frac{1}{6}u_{kl}u_{qr} - \frac{1}{6}u_{kl}u_{ql} \right] - U_\infty \left( \frac{1}{2}u_{0r} - \frac{1}{2}u_{0l} \right) \\ \sum_{k,q=0}^{N_r} C_{k,q,1} \left[ \frac{1}{3}u_{kr}u_{qr} - \frac{1}{3}u_{kr}u_{ql} + \frac{1}{6}u_{kl}u_{qr} - \frac{1}{6}u_{kl}u_{ql} \right] - U_\infty \left( \frac{1}{2}u_{0r} - \frac{1}{2}u_{0l} \right) \\ \vdots \\ \sum_{k,q=0}^{N_r} C_{k,q,N_r} \left[ \frac{1}{3}u_{kr}u_{qr} - \frac{1}{3}u_{kr}u_{ql} + \frac{1}{6}u_{kl}u_{qr} - \frac{1}{6}u_{kl}u_{ql} \right] - U_\infty \left( \frac{1}{2}u_{0r} - \frac{1}{2}u_{0l} \right) \end{bmatrix} \quad (3.40)$$

The last term to be written out is the other nonlinear term. The derivation starts with the integral formulation of the equation:

$$\frac{\partial U(x, r)}{\partial r} V(x, r) \quad (3.41)$$

Now introducing the Galerkin projection and rewriting the term in the weak formulation:

$$\begin{aligned} \int_{x_l}^{x_r} \int_0^\infty \frac{\partial U(x, r)}{\partial r} V(x, r) r \, dr \, dx &= \int_0^\infty \int_{x_l}^{x_r} \sum_{k,q=0}^{N_r} \frac{1}{r} \psi_m(r) \psi'_k(r) (1 - \psi_q(r)) \\ &\quad \frac{x - x_l}{x_r - x_l} \left[ \frac{x - x_l}{x_r - x_l} u_{kr} + \frac{x_r - x}{x_r - x_l} u_{kl} \right] \left[ \frac{x - x_l}{x_r - x_l} v_{qr} + \frac{x_r - x}{x_r - x_l} v_{ql} \right] r \, dr \, dx \end{aligned} \quad (3.42)$$

In a similar manner to the previous equations, the x-terms are integrated first.

$$\int_{x_l}^{x_r} \frac{x - x_l}{x_r - x_l} \left[ \frac{x - x_l}{x_r - x_l} u_{kr} + \frac{x_r - x}{x_r - x_l} u_{kl} \right] \left[ \frac{x - x_l}{x_r - x_l} v_{qr} + \frac{x_r - x}{x_r - x_l} v_{ql} \right] dx = \quad (3.43)$$

$$\Delta x \left( \frac{1}{4} u_{kr} v_{qr} + \frac{1}{12} u_{kl} v_{qr} + \frac{1}{12} u_{kr} v_{ql} + \frac{1}{12} u_{kl} v_{ql} \right) \quad (3.44)$$

Writing out the radial derivatives accordingly to equation (2.47)

$$\begin{aligned}
\int_0^\infty \sum_{k,q=0}^{N_r} \psi_m(r) \psi'_k(r) (1 - \psi_q(r)) dr &= \int_0^\infty \sum_{k,q=0}^{N_r} r \psi_m(r) \left( \psi_k(r) \right. \\
&\quad \left. + 2 \sum_{i=0}^{k-1} \psi_i(r) \right) (1 - \psi_q(r)) dr \\
&= \int_0^\infty \sum_{k,l,m=0}^{N_r} \psi_m(r) \left( \psi_k(r) + 2 \sum_{i=0}^{k-1} \psi_i(r) \right) r \\
&\quad - \psi_q(r) \psi_m(r) \left( \psi_k(r) + 2 \sum_{i=0}^{k-1} \psi_i(r) \right) r dr
\end{aligned}$$

Applying the orthogonality relation where applicable and expressing the integrals in the triple integral notation of equation (2.52):

$$\int_0^\infty \sum_{k,q=0}^{N_r} \psi_m \psi'_k(r) (1 - \psi_q) dr = \sum_{k,q=0}^{N_r} \delta_{k,m} - C_{k,q,m} + 2 \sum_{i=0}^{k-1} \delta_{i,m} - 2C_{i,q,m} \quad (3.45)$$

The complete equation then becomes:

$$\begin{aligned}
\iint_{\Omega} b(x,r) \frac{\partial U(x,r)}{\partial r} V(x,r) dV &= \Delta x \left( \sum_{k,q=0}^{N_r} \delta_{k,m} - C_{k,q,m} + 2 \sum_{i=0}^{k-1} \delta_{i,m} \right. \\
&\quad \left. - 2C_{i,q,m} \right) \left( \frac{1}{4} u_{kr} v_{qr} + \frac{1}{12} u_{kl} v_{qr} + \frac{1}{12} u_{kr} v_{ql} + \frac{1}{12} u_{kl} v_{ql} \right) \quad (3.46)
\end{aligned}$$

Thus, the functional matrix with its rows corresponding to the radial indices of the projection becomes:

$$\Delta x \begin{bmatrix} \sum_{k,q=0}^{N_r} \left( \delta_{k,0} - C_{k,q,0} + 2 \sum_{i=0}^{k-1} \delta_{i,0} - C_{i,q,0} \right) \\ \left( \frac{1}{4} u_{kr} v_{qr} + \frac{1}{12} u_{kl} v_{qr} + \frac{1}{12} u_{kr} v_{ql} + \frac{1}{12} u_{kl} v_{ql} \right) \\ \sum_{k,q=0}^{N_r} \left( \delta_{k,1} - C_{k,q,1} + 2 \sum_{i=0}^{k-1} \delta_{i,1} - C_{i,q,1} \right) \\ \left( \frac{1}{4} u_{kr} v_{qr} + \frac{1}{12} u_{kl} v_{qr} + \frac{1}{12} u_{kr} v_{ql} + \frac{1}{12} u_{kl} v_{ql} \right) \\ \vdots \\ \sum_{k,q=0}^{N_r} \left( \delta_{k,N_r} - C_{k,q,N_r} + 2 \sum_{i=0}^{k-1} \delta_{i,N_r} - C_{i,q,N_r} \right) \\ \left( \frac{1}{4} u_{kr} v_{qr} + \frac{1}{12} u_{kl} v_{qr} + \frac{1}{12} u_{kr} v_{ql} + \frac{1}{12} u_{kl} v_{ql} \right) \end{bmatrix} \quad (3.47)$$

Even though all terms have been worked out, the result can still not be directly computed. This requires a solver to handle the nonlinear terms.

### 3.2.3 Nonlinear Solver

A nonlinear solver must be employed to solve the equation's nonlinear terms. Newton Rhapson's method (3.48) is applied to this system of equations. The method relies on a Jacobian of the system to come to the next step of iteration. The Jacobian of the system will be similar to matrix (3.49). The first index of the subscript of the function  $f$  indicates whether the function belongs to the mass ( $f_{0,0}$ ) or momentum equation ( $f_{1,0}$ ). The second index corresponds to the index of the projection function. Typically, the projection function is described by its radial and axial index. In the Jacobian these combine into one integer, starting at the axial index.

$$\begin{pmatrix} U_i^{n+1} \\ V_i^{n+1} \end{pmatrix} = \begin{pmatrix} U_i^n \\ V_i^n \end{pmatrix} - J(U_i^n, V_i^n)^{-1} f(U_i^n, V_i^n) \quad (3.48)$$

$$J(U_i^n, V_i^n) = \begin{bmatrix} \frac{\partial f_{0,0}}{\partial u_0} & \frac{\partial f_{0,0}}{\partial u_1} & \frac{\partial f_{0,0}}{\partial u_2} & \cdots & \frac{\partial f_{0,0}}{\partial v_{N_r-2}} & \frac{\partial f_{0,0}}{\partial v_{N_r-1}} & \frac{\partial f_{0,0}}{\partial v_{N_r}} \\ \frac{\partial f_{0,1}}{\partial u_0} & \frac{\partial f_{0,1}}{\partial u_1} & \frac{\partial f_{0,1}}{\partial u_2} & & \frac{\partial f_{0,1}}{\partial v_{N_r-2}} & \frac{\partial f_{0,1}}{\partial v_{N_r-1}} & \frac{\partial f_{0,1}}{\partial v_{N_r}} \\ \frac{\partial f_{0,2}}{\partial u_0} & \frac{\partial f_{0,2}}{\partial u_1} & \frac{\partial f_{0,2}}{\partial u_2} & & \frac{\partial f_{0,2}}{\partial v_{N_r-2}} & \frac{\partial f_{0,2}}{\partial v_{N_r-1}} & \frac{\partial f_{0,2}}{\partial v_{N_r}} \\ \vdots & & & \ddots & & & \vdots \\ \frac{\partial f_{0,N_r}}{\partial u_0} & \frac{\partial f_{0,N_r}}{\partial u_1} & \frac{\partial f_{0,N_r}}{\partial u_2} & & \frac{\partial f_{0,N_r}}{\partial v_{N_r-2}} & \frac{\partial f_{0,N_r}}{\partial v_{N_r-1}} & \frac{\partial f_{0,N_r}}{\partial v_{N_r}} \\ \frac{\partial f_{1,0}}{\partial u_0} & \frac{\partial f_{1,0}}{\partial u_1} & \frac{\partial f_{1,0}}{\partial u_2} & & \frac{\partial f_{1,0}}{\partial v_{N_r-2}} & \frac{\partial f_{1,0}}{\partial v_{N_r-1}} & \frac{\partial f_{1,0}}{\partial v_{N_r}} \\ \vdots & & & \ddots & & & \vdots \\ \frac{\partial f_{1,N_r-1}}{\partial u_0} & \frac{\partial f_{1,N_r-1}}{\partial u_1} & \frac{\partial f_{1,N_r-1}}{\partial u_2} & \cdots & \frac{\partial f_{1,N_r-1}}{\partial v_{N_r-2}} & \frac{\partial f_{1,N_r-1}}{\partial v_{N_r-1}} & \frac{\partial f_{1,N_r-1}}{\partial v_{N_r}} \end{bmatrix} \quad [2N_r \times 2N_r] \quad (3.49)$$

All linear terms from the two equations have a straightforward implementation because the derivative of a linear term is a constant. The derivatives of the nonlinear terms, retain a dependency on the variables  $U$  and  $V$ .

Equation (3.48) helps determine the stopping criterion. The residual tolerance for convergence is set to  $1e-6$  and is defined by the absolute value of  $J(U_i^n, V_i^n)^{-1} f(U_i^n, V_i^n)$ .

# Chapter 4

## Verification

Before considering the model's results, two tests are performed to assess the discretization. The first test is for the diffusion equation, described in section 4.1. Considering the diffusion term is essentially the heat equation, much is known about its outcome and its behavior. Section 4.2 contains the results for the tests of both the mass and momentum terms.

### 4.1 Diffusion Equation

This section should be taken as an isolated test, that is used as a verification for the diffusion term. The equations discussed here will not be included in the model and a discretization in time only sees implementation for this test. The purpose of this test is to assess the correctness of the radial discretization and get an error estimate for the radial discretization. The equation used as an example for this case is:

$$\frac{\partial U(r)}{\partial t} = \nu_T \nabla \cdot (\nabla U(r)) \quad (4.1)$$

Previously, a velocity expression dependent on radial and downstream basis functions was used to model the equations. A velocity expression dependent on time, supported by a radial basis function is employed for this equation. The motivation for these dimensions comes from the need for verification of the radial basis functions. Taking an expression for the velocity with the adjusted Laguerre functions(2.37,  $\psi$ ):

$$U = \sum_k^{N_r} U_k(t) \psi_k \quad (4.2)$$

Naturally, the accompanying projection function exists of:

$$b_m = \psi_m(r) \quad (4.3)$$

To support diffusion and to visualize the effect, an explicit Euler method (equation (4.4)) is employed. Do note the superscript is used as an indication of the marching step:

$$\frac{\partial U(r)}{\partial t} = \frac{U^{i+1}(r) - U^i(r)}{h_t} \quad (4.4)$$

Rewriting equation (4.1) with equation (4.4) provides the marching expression (4.5). The  $\nabla$ -operator used throughout this section is only one-dimensional, hence, the expression in its weak formulation simplifies down to equation (4.6).

$$b_m(r)U^{i+1}(r) = b_m(r)U^i(r) + h_t\nu_T b_m(r)\nabla \cdot (\nabla U^i(r)) \quad (4.5)$$

$$\int_0^\infty b_m(r)U^{i+1}(r) dr = \int_0^\infty b_m(r)U^i(r) dr + h_t\nu_T \int_0^\infty \frac{\partial b_m(r)}{\partial r} \frac{\partial V(r)}{\partial r} dr \quad (4.6)$$

The last term,  $\int_0^\infty \frac{\partial b_m(r)}{\partial r} \frac{\partial V(r)}{\partial r}$ , is the same as in equation (3.31), which allows plugging in the same expression as derived before while neglecting its x-discretization. This brings the two other terms to be solved. Without taking any derivatives of the functions, the terms can be straightforwardly subjected to the orthogonality relation (2.40), thus, the final expression reads:

$$\int_0^\infty b_m(r)U^i(r) dr = \sum_{k=0}^{N_r} U_k^i \int_0^\infty \psi_k \psi_m dr = \frac{1}{2} \sum_{k=0}^{N_r} U_k^i \delta_{k,m} \quad (4.7)$$

$$\sum_{k=0}^{N_r} U_k^{i+1} \delta_{k,m} = \sum_{k=0}^{N_r} U_k^{i+1} \delta_{k,m} - h_t\nu_T \sum_{k=0}^{N_r} (2k+1)\delta_{k,m} + k\delta_{k-1,m} + m\delta_{k,m-1} \quad (4.8)$$

The discretization choice with respect to time has many consequences in its own right, but those shall be left out for this test as they are not the focus here. Instead, the conservation error due to the discretization in the radial direction is what is being tested.

Assessing the error for the implementation of the diffusion equation requires a few steps. The approach relies on the continuity of mass flux. The integral should yield the same constant for the entire domain, regardless of how far the equation has marched down in time. The general expression for the error derived from the integral property reads:

$$\sum_{k=0}^{N_r} U_k \int_0^\infty \psi_k(r) r dr = \sum_{k=0}^{N_r} U_k \int_0^\infty \psi_k(r) r dr \quad (4.9)$$

$$\varepsilon_t = \left| \sum_{k=0}^{N_r} U_k^{t=0} \int_0^\infty \psi_k(r) r dr - \sum_{k=0}^{N_r} U_k^t \int_0^\infty \psi_k(r) r dr \right| \quad (4.10)$$

Solving the integral is obtained by induction from equation (3.6) and taking the limits of  $r$ . The first integral derived is for the zeroth order, which can easily be computed by evaluating the integral;

$$\int_0^\infty \psi_0(r) r dr = \lim_{r \rightarrow \infty} \underbrace{[1 - \psi_0(r)]}_{=1} - \underbrace{1 - \psi_0(r)}_{=0} = 1 \quad (4.11)$$

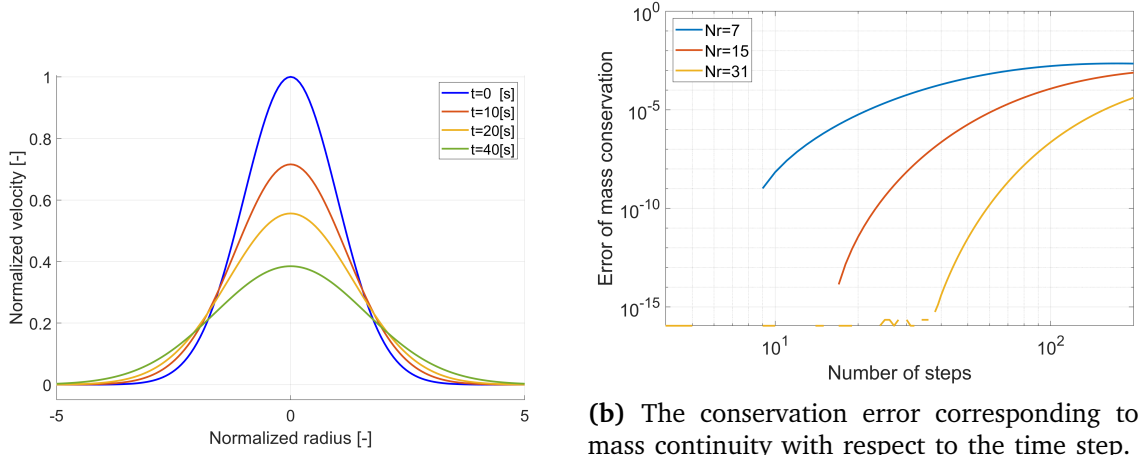
Evaluating the integral for each integral belonging to a higher-order term yields either -1 or 1, hence, the definite integral over the domain becomes:

$$\int_0^\infty \psi_n(r) r dr = (-1)^n \quad (4.12)$$

Now that the integral can be solved, the error can be assessed. The last step before computations can be performed is to fix the constants for the test. The initial condition chosen for the test is that of a Gaussian ( $e^{-\frac{r^2}{2}}$ ). The motivation behind this choice is that the lowest-order Laguerre function resembles a Gaussian, meaning that the initial condition requires no fitting. Other parameters which are fixed for the computation are the time step  $h_t$  which is set to 1, the viscosity,  $\nu_T = 2 \cdot 10^{-3}$ , and the initial velocity coefficient which is set to 1.

The result of the computation is shown in figure 4.1a, showing the dissipation of the initial Gaussian shape for the equations modeled by 16 radial modes. The diffusion of the velocity follows a typical diffusion pattern and matches the expectations, indicating a minimal error and, consequently, a correct implementation of the diffusion equation. Expansion of the profile in the radial direction is limited due to the exponential decay of the basis.

The minimal error claim is supported by figure 4.1b. Noticeably, the error remains zero until it quickly increases. What is most interesting is the difference between the number of steps required for the error to increase with respect to the number of radial modes. This suggests a higher number of radial modes are able to model the diffusion accurately for more steps. The matrix belonging to the radial diffusion expression (3.32) indicates a coefficient relies on its neighbors that are only one position



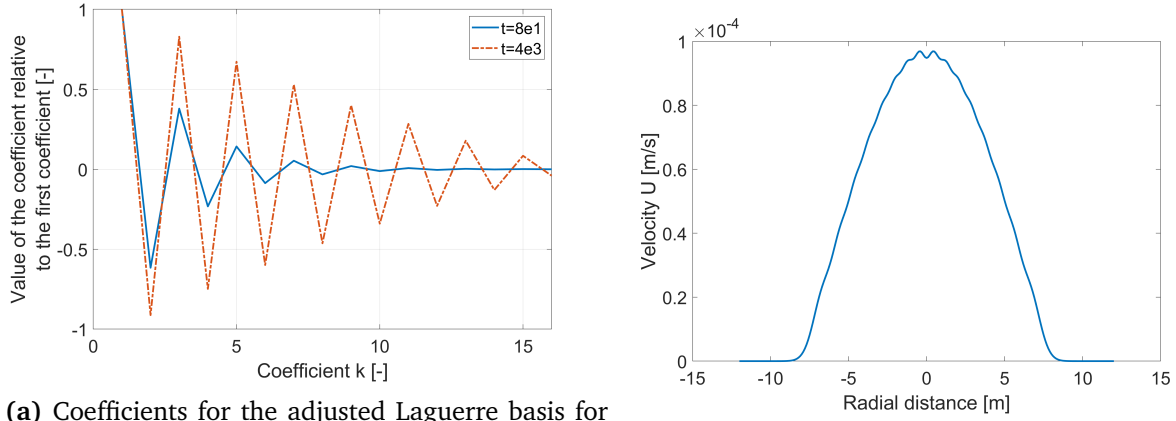
(a) The velocity profile of the initial Gaussian profile three different lines correspond to different numbers propagated through time for the diffusion equation. of radial modes in the domain.

**Figure 4.1:** The results for the tests of the radially discretized diffusion term with an adjusted Laguerre function support.

away. This means that the highest orders will only be engaged in the model at  $N_r$  steps and then slowly increase. Once the higher orders are fully engaged the error begins to rapidly increase, suggesting truncation of the available modes to be the root of this error. Conceptually, the error can be compared to a FE approach hitting the domain boundary, information is lost to the system because the basis does not reach that far. This loss of information is supported by figure 4.2a, which shows the relative dependency on the higher order terms and relation to the error. The velocity profile accompanying these coefficients is shown in figure 4.2b. Do note that the profile has already diffused leading to a lower velocity profile. Quantitatively, the amplitude of the solution is lower by approximately  $10^4$ , however, the solution still distinctly resembles the shape of a Gaussian.

## 4.2 Full System of Equations

In a similar fashion, the entire system of equations can be tested. The two different errors computed to assess the model are based on the continuity of mass (3.2) and the continuity of momentum (2.13). Differently from developing the model, the integrals do not correspond to the weak formulation of the problem. Instead, the integrals correlate to the conservation of mass and momentum for each step. Evaluating the continuity at downstream steps should be done by integrating the azimuthal dimension and the radial dimension. This approach relies on employing the divergence theorem



(a) Coefficients for the adjusted Laguerre basis for the modeled diffusion equation at the start of the error ( $t = 8e1$ ) and a developed error ( $t = 4e3$ ). Ob- a visual example of erroneous Laguerre projections. tained for 16 radial modes. (b) Velocity profile at  $t = 4e3$ . Modeled with 16 radial modes.

**Figure 4.2:** The visualization of the velocity coefficients and the velocity profile at higher errors

(Anderson [2017]) to come to the following notation:

$$\iint_{\Omega} \nabla \cdot \begin{bmatrix} U(x, r) \\ V(x, r) \end{bmatrix} dV = \oint_{\partial\Omega} \vec{n} \cdot \begin{bmatrix} U(x, r) \\ V(x, r) \end{bmatrix} dA \quad (4.13)$$

Evaluating the surface integrals will only yield results in the axial dimension (4.15, 4.16), following the fact that the radial velocity is zero for its respective boundary integral (4.14). Thus, the mass continuity is described by equation (4.17).

$$\lim_{r \rightarrow \infty} \oint_{\partial\Omega_3} \begin{bmatrix} 0 \\ 1 \end{bmatrix} \begin{bmatrix} U(x, r) \\ V(x, r) \end{bmatrix} dA = 0 \quad (4.14)$$

$$\oint_{\partial\Omega_2} \begin{bmatrix} -1 \\ 0 \end{bmatrix} \begin{bmatrix} U(x_l, r) \\ V(x_l, r) \end{bmatrix} dA = -U_k(x_l) \int_0^\infty \psi_k(r) r dr \quad (4.15)$$

$$\oint_{\partial\Omega_1} \begin{bmatrix} 1 \\ 0 \end{bmatrix} \begin{bmatrix} U(x_r, r) \\ V(x_r, r) \end{bmatrix} dA = U_k(x_r) \int_0^\infty \psi_k(r) r dr \quad (4.16)$$

$$\oint_{\partial\Omega} \vec{n} \cdot \begin{bmatrix} U(x, r) \\ V(x, r) \end{bmatrix} dA = \sum_{k=0}^{N_r} (U_k(x_r) - U_k(x_l)) \int_0^\infty \psi_k(r) r dr \quad (4.17)$$

Equation (4.12) contains the solution to the definite integral for a single adjusted Laguerre function, from which the final expression of the mass equation can be defined:

$$\text{Constant} = \sum_{k=0}^{N_r} (U_k(x_r) - U_k(x_l)) (-1)^k dr \quad (4.18)$$

Continuity of momentum forms another basis to assess the error of the implementation. Arriving at the error formulation for the conservation of momentum requires more arithmetic effort than for the mass error. Because the focus of these tests is not motivated by the need to model any physical phenomenon, the viscosity is a fixed viscosity set to  $2 \cdot 10^{-2}$ . Evaluating the momentum equation in its integral form yields the first step:

$$\int_{\Omega} \frac{\partial U(x, r)}{\partial x} U(x, r) dV + \int_{\Omega} \frac{\partial V(x, r)}{\partial r} U(x, r) dV = \nu_T \int_{\Omega} \nabla \cdot (\nabla U(x, r)) dV \quad (4.19)$$

$$\int_{\Omega} \frac{\partial U(x, r)}{\partial x} U(x, r) dV + \int_{\Omega} \frac{\partial V(x, r)}{\partial r} U(x, r) dV = \nu_T \int_{\Omega} \left( \frac{\partial^2 U(x, r)}{\partial x^2} + \frac{1}{r} \frac{\partial}{\partial r} \frac{\partial U(x, r)}{\partial r} \right) dV \quad (4.20)$$

The basis in the downstream direction is piecewise linear, hence, its second derivative is zero, reducing  $\frac{\partial^2 U(x, r)}{\partial x^2}$  to zero straightaway. The radial derivative of the diffusion term requires a bit more effort. Evaluating the volume integral results:

$$\nu_T \int_{x_l}^{x_r} \int_0^\infty \frac{1}{r} \frac{\partial}{\partial r} \frac{\partial U(x, r)}{\partial r} r \, dr \, dx = \nu_T \int_{x_l}^{x_r} \left[ \frac{\partial U(x, r)}{\partial r} \right]_0^{r \rightarrow \infty} dx \quad (4.21)$$

$$\left[ \frac{\partial U(x, r)}{\partial r} \right]_0^{r \rightarrow \infty} = \underbrace{\lim_{r \rightarrow \infty} (r \psi_k U_k(x))}_{=0} - 0 = 0 \quad (4.22)$$

Now that the diffusion term has been removed completely, the terms on the left-hand side are to be worked out. The advection term can alternatively be expressed as a divergence of the velocities terms, which allows for, yet again, the divergence theorem to be applied:

$$\int_{\Omega} \nabla \cdot \left( \begin{bmatrix} U(x, r) \\ V(x, r) \end{bmatrix} U(x, r) \right) dV = \int_{\partial\Omega} \vec{n} \cdot \left( \begin{bmatrix} U(x, r) \\ V(x, r) \end{bmatrix} U(x, r) \right) dA \quad (4.23)$$

Similarly to the previous implementations of the divergence theorem, there are three different boundaries to evaluate the integrals with respect to. The first two are in the axial direction; upstream and downstream. The last boundary is for  $r \rightarrow \infty$ . The results of these integrals are:

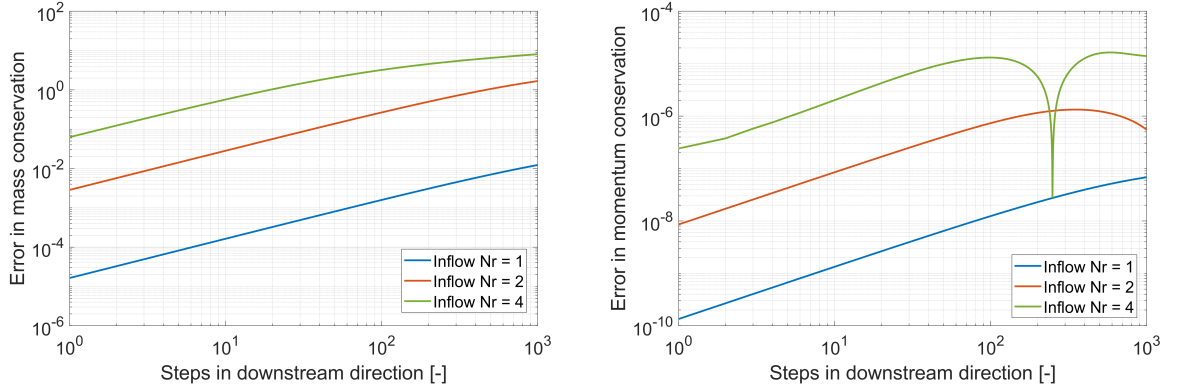
$$\int_{\partial\Omega_1} \begin{bmatrix} 1 \\ 0 \end{bmatrix} \cdot \left( \begin{bmatrix} U(x_r, r) \\ V(x_r, r) \end{bmatrix} U(x_r, r) \right) dA = \int_0^\infty \sum_{k,q=0}^{N_r} U_k(x_r) U_q(x_r) \psi_k \psi_q r \, dr \quad (4.24)$$

$$= \sum_{k,q=0}^{N_r} U_k(x_r) U_q(x_r) \delta_{k,q} \quad (4.25)$$

$$\int_{\partial\Omega_2} \begin{bmatrix} -1 \\ 0 \end{bmatrix} \cdot \left( \begin{bmatrix} U(x_l, r) \\ V(x_l, r) \end{bmatrix} U(x_l, r) \right) dA = \int_0^\infty \sum_{k,q=0}^{N_r} U_k(x_l) U_q(x_l) \psi_k(r) \psi_q(r) r \, dr \quad (4.26)$$

$$= - \sum_{k,q=0}^{N_r} U_k(x_l) U_q(x_l) \delta_{k,q} \quad (4.27)$$

$$\int_{\partial\Omega_2} \begin{bmatrix} 0 \\ 1 \end{bmatrix} \cdot \left( \begin{bmatrix} U(x, r) \\ V(x, r) \end{bmatrix} U(x, r) \right) dA = \int_0^\infty \sum_{k,q=0}^{N_r} U_k(x) U_q(x) \underbrace{\lim_{r \rightarrow \infty} \psi_k(r) \psi_q(r)}_{=0} dx \quad (4.28)$$



(a) The error in the continuity of mass with respect to the start of the domain. (b) The conservation of momentum error with respect to the start of the domain.

**Figure 4.3:** Error results for a fixed number of radial modes for the domain with differing numbers of radial modes used to model the inflow. The simulations were performed with 8 radial modes in the domain.

Combining these expressions yields the expression for the conservation of momentum. This expression thus reads:

$$\text{Constant} = U_r^2 - U_l^2 \quad (4.29)$$

The error in momentum is computed by taking the relative difference in constant at a downstream position with respect to the inflow. This is what constitutes the error for this continuity.

Although the model has been developed to model wake flows, it too can be subjected to any input. For the test case, the inflow is set to a certain number of coefficients. The number of radial modes used for the inflow indicates how many of the first coefficients are nonzero, starting from the lowest-order coefficient. The nonzero elements are set to one.

Unlike the linear diffusion equation, the model will, from the first step in the simulation, engage all coefficients. This is a property of the method applied, yet, the biggest coefficients will not directly play a major role. The limitations of equation (2.52) set the number of radial modes to 8. Additionally, they are likely to contribute to the error in the system too.

The slope of the error shows an order of  $\sqrt{N}$ , which is not problematic, however, the starting error is much higher than acceptable. In figure 4.3b a dip can be seen. This is only an indication of a change of sign and does not indicate any other phenomenon.

Another noteworthy aspect would be the difference between figure 4.3 and figure 4.1. Figure 4.3 shows no sudden jump in error due to truncation over the tested domain. Considering the results are obtained with only 8 radial modes, some consequence of truncation similar to figure 4.1b is expected. This indicates that the error is either already so high that it is barely affected, or that the truncation error is present from the very start of computations. The truncation error seems to be the most likely candidate for the error, as the slope of the error remains unaffected, and the starting error increases for an increase in inflow modes. This suggests that a higher number of modes may even be required to model the lowest possible number of inflow modes within machine precision.

[This page is intentionally left blank]

# Chapter 5

## Wake Analysis

The application of the method and the chosen domain can be found in chapter 3, worked out in a flowchart (5.1). The model also allows for the emission of the step to compute the viscosity for every iteration in Newton-Rhapson's method. By prescribing an eddy viscosity for the entire domain, the model may be sped up too. Due to the nature of the spectral method's superposition property, the velocity field must be computed for the domain every time the minimum velocity is required.

In this section, the design of the complete model and its results are analyzed and discussed. The findings are taken up in the recommendations for further research.

### 5.1 The Modelled Boundary Conditions

The inflow conditions associated with the wake serve as a reliable indicator for determining the number of radial modes necessary for an accurate model. As the flow progresses downstream, the velocity profile converges towards a Gaussian distribution, as documented by Vermeer et al. [2003]. A Gaussian profile can be effectively modeled utilizing Laguerre functions, thus the inflow is the more concerning aspect of the flow.

To compute the inflow velocity profile, data from the DTU 10MW reference wind turbine (Bak et al. [2013]) was used as input data to a BEM model by Siemens Gamesa. The output of the BEM was further padded with the freestream velocity. The resulting velocity profile is exclusively provided in the axial direction. In order to provide a complete Dirichlet boundary condition, the inflow data is expanded with zeros for the radial velocity coefficients.

Laguerre functions tend to zero when approaching infinity. Unfortunately, the speed with which the functions tend to zero differs for each order. To accommodate this difference, the domain is scaled for different numbers of radial modes. The scaling is done by visually inspecting the functions and basing the scaling on when the highest-

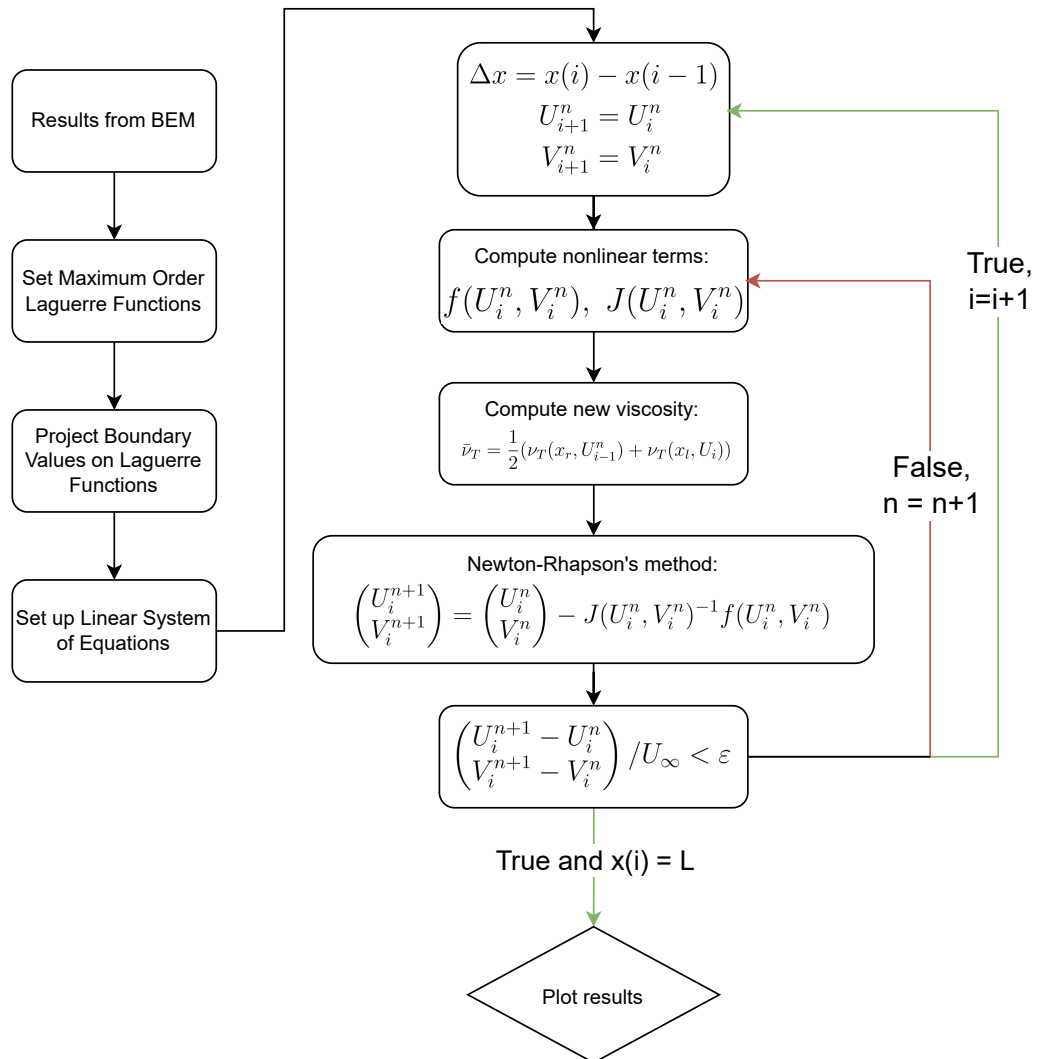


Figure 5.1: Flow of the script with its iterative convergence scheme colorized.

**Table 5.1:** Scaling parameters and the corresponding error for different numbers of radial modes fitted to the inflow conditions.

$N_r$	Scale	RMS
7	8	0.5627
15	22	0.3219
31	52	0.1889
63	110	0.1275

order function is nearing zero. Doing this for many different radial modes is time-consuming and unnecessary, so the scaling has only been done for a select number of radial modes.

To assess the fit numerically, the RMS error for the different number of radial modes is assessed. The size of the tested domain affects the outcome of the RMS error, thus, the domain goes up when the lowest radial mode has converged to the free stream velocity with a margin of  $1e^{-6}$ , shown in table 5.1, with the corresponding scaling parameter. The projected inflow may be found in figure 5.2.

Many disciplines would prefer to have no overshoot at the end of the fitted domain, whereas, for wind turbine wakes, the overshoot matches the physical reality of the flow. This cannot be quantitatively assessed, due to the limited domain of the BEM, thus, the overshoot can only be said to be qualitatively correct.

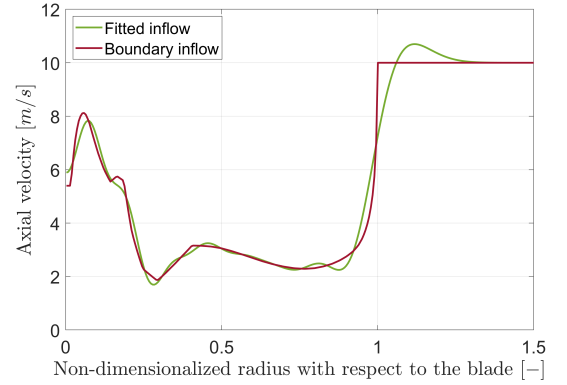
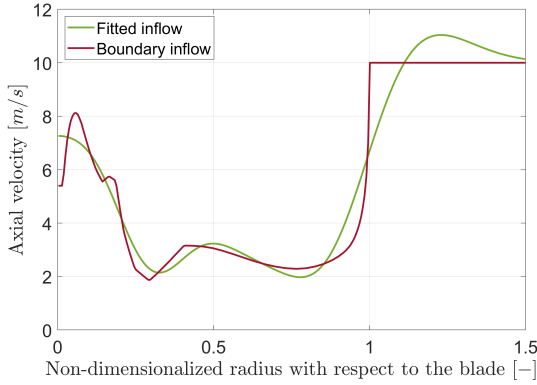
Starting at the lowest number of radial modes (figure 5.2a), the projection strongly resembles the shape of Laguerre functions instead of the shape of the inflow. As expected, the lowest order method corresponds to the biggest error.

The second-lowest number of radial modes (figure 5.2b) shows better accordance with the inflow velocity profile. More features of the inflow velocity profile are taken up into the projection and its error is significantly lower than.

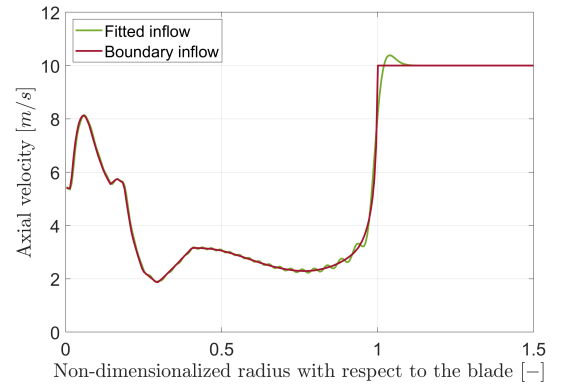
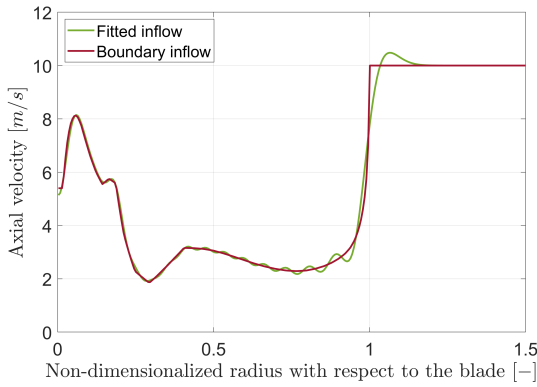
## 5.2 Wake Expansion

The scaling requirements suggest a fixed number of radial modes corresponding to a fixed wake radius. To accommodate for an expansion of the investigated domain, a higher number of modes is used for the modeling than for the boundary fit. By taking double the modes of the boundary inflow, the flow downstream may be more enticed to expand. Even though the current implementation of equation (2.52) does not accommodate a consistent output for an order of 15, the wake model will use 16 radial modes to double the number of modes compared to the inflow wake.

Figure 5.3a and 5.3b show the wakes for, respectively, 8 radial modes and 16 radial modes. Both results are obtained for a fixed eddy viscosity ( $\bar{\nu}_T = 8e^{-3}$ ).



(a) The BEM result projected onto 8 radial modes (b) The BEM result projected onto 15 radial modes



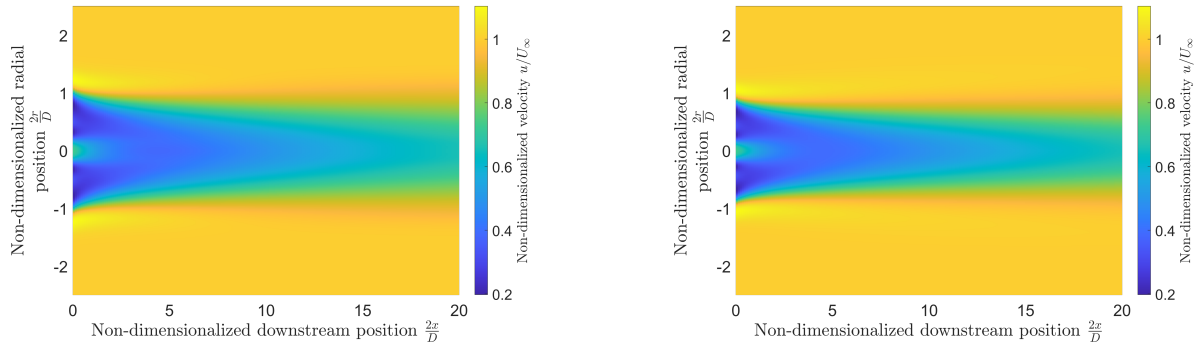
(c) The BEM result projected onto 32 radial modes (d) The BEM result projected onto 64 radial modes

**Figure 5.2:** Boundary inflow projected onto basis functions for different numbers of radial modes

Regarding the lower-order wake model, it is important to note that, by the definition of the wake expansion  $U_{min} = 99\% U_{inf}$ , the initial wake is already at a radius of  $1.11D$ , which can be visually reaffirmed with figure 5.2a. This means that the relative expansion is less, however, it does not mean the wake expansion is insignificant. Especially, when considering the wake expansion for  $N_r = 15$ , which starts at the same wake expansion as  $N_r = 7$ . The wake expands up to  $1.35$  diameters.

Still, one cannot claim that using more radial modes in the model than at the boundary fit, leads to an under-expanded wake. The numerical error coming from the explicit triple Laguerre makes any claims regarding such flow phenomenon impossible.

The script as is, will not converge for  $N_r = 15$  without fewer modes at the boundary condition. Simulations for  $N_r \leq 11$  have converged without failure.



(a) The resulting wake with a similar amount of modes at the inflow as the domain for 8 radial modes. The wake expands to  $0.81D$ .

(b) The resulting wake with 16 radial modes in the domain and 8 radial modes at the inflow. The wake expands to  $0.7D$ .

**Figure 5.3:** The resulting wakes both for a prescribed viscosity of  $8e^{-3}$

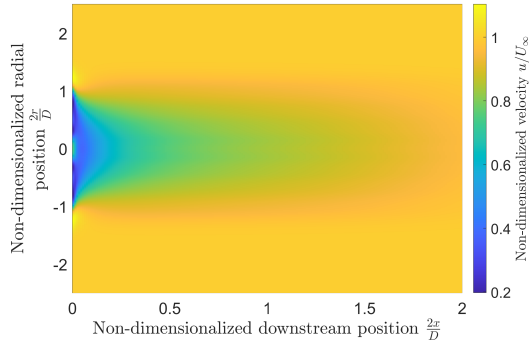
## 5.3 Eddy Viscosity Effects

A critical aspect of the applied wake model is the prescribed viscosity equation and its implementation. Computing the averaged vorticity for each step will affect wake diffusion significantly. The empirically fitted viscosity equation is intended to provide a wake more in line with real-world experiments. The result for a viscosity, based on the viscosity equation as described in equation (2.14), is shown in figure 5.4a. The viscosity accompanying the same domain is shown in figure 5.4b. Do note the domain has been shortened to create a useful image, as the wake has mostly diffused beyond 2 diameters downstream.

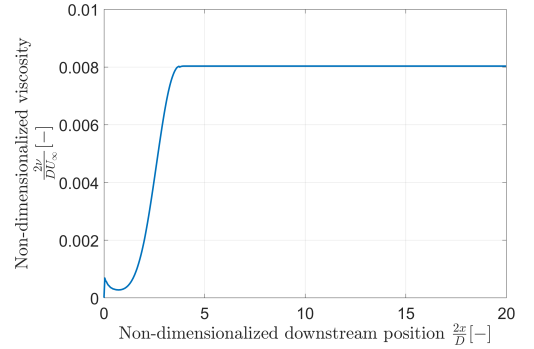
The result cannot be directly compared to examples in literature with similar implementations unless the conditions are matched. However, a superficial comparison to the implementation by Reinwardt et al. [2019], suggests that the model heavily overestimates diffusion of the wake.

Nevertheless, some things may still be discussed about the result. First of all, the viscosity remains constant from  $x/D = 4$ . This makes sense when we take a look at equation (2.14) since the term dependent on the relative wake velocity with respect to the flow has decreased to zero. The viscosity term thereby solely depends on the ambient viscosity. A potential root of the overestimate may be the scaling parameters from the input flow fit, yet, that is unlikely to scale the viscosity by so much that it completely dissipates within 2 diameters.

Moreover, there is barely any wake expansion visible. It should again be noted that the simulation has been performed for an equal number of radial modes downstream as for the inflow fit.



(a) The resulting wake for with a similar number of inflow modes as modes in the domain, for  $N_r = 7$ .



(b) Non-dimensionalized  $\nu_T$  with respect to non-dimensionalized axial position  $\tilde{x}$ .

**Figure 5.4:** The results of the wake model with the eddy viscosity equation implemented for each downstream step, for  $I_{amb} = 3e - 2$

Compared to other parts of the script, the computation of the eddy viscosity for each step is the most computationally expensive. This is an unavoidable aspect of the method. To compute the lowest velocity and the wake radius, the velocity field must be constructed from the superposition of the Laguerre functions with their respective coefficients.

## 5.4 Conservation Error

To assess the model's performance for actual modeling, the same errors are computed as in section 4.2. The errors are described by equation (4.18) and equation (4.29). The ideal outcome would have a result close to machine precision, however, as already discussed in chapter 4, there is an extra error source. From figure 5.5 it is apparent the error is larger than the machine precision error. The error plots are in accordance with the highest inflow error plots in figure 4.3. This is consistent with the relative ratio of domain modes and inflow modes. This suggests that the shape of the inflow does not lead to a significant increase in conservation error, moreover, the cut-off error as seen in figure 4.1b may be present from the very start of the domain. This may be the result of the connectivity for the velocity coefficients in the system of equations.

Increasing the number of modes does yield a lower error, even though, the explicit triple product integrals could form an additional significant error source for higher modes. It would be interesting to check it for even higher terms, but that is limited by higher orders not converging to a solution.

Noteworthy, the error in mass conservation is higher than the error in momentum

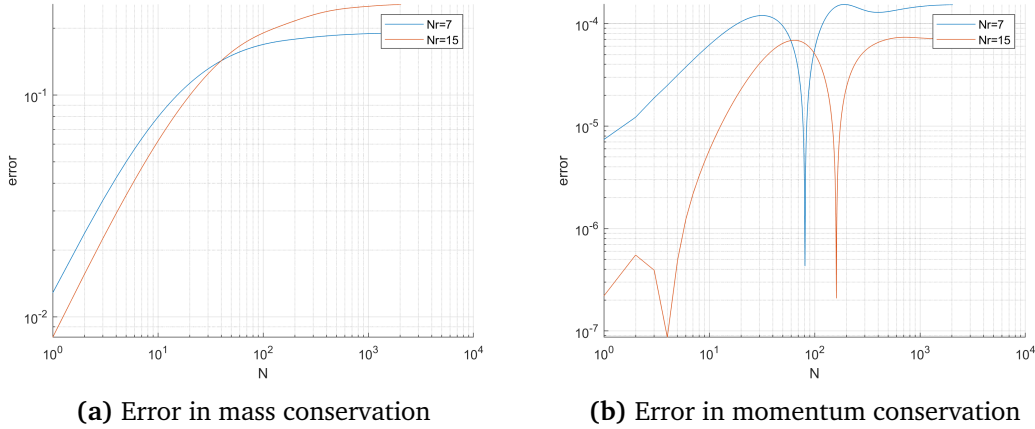


**Figure 5.5:** Errors in the final results for the conservation of mass and momentum. The domain

conservation. This happened again in accordance with figure 5.5, but should still be noted. It may be argued that the difference originates from the high starting error for the mass conservation as the trend is otherwise of the same order. This may be because the mass error is most affected by the cut-off error.

Another potential source that affects the result is the error threshold for the Newton-Rhapson iterations. The solution would not converge for error tolerances higher than  $1e^{-12}$ , indicating there is already an error source that would not allow the Newton-Rhapson to be computed. A lower error tolerance in the solver leads to a higher eventual error for the system and should be considered as an additional root. Typically, one could also consider numerical round-off errors, however, those are relatively small and are not a practical addition to this discussion.

As discussed in section 2.3.5, the implementation of the explicit triple product integral comes with a high error. Additionally, the material to validate the outcome only goes up to the 10th order with a precision of 8 digits. Validating higher modes by hand was too time-consuming and error-prone, yet, quantifying the error could be approached by comparing the terms that should be symmetric. By taking the highest error, described by equation (5.1), in the symmetric for each order the content of table 5.2 may be computed. The error equation essentially represents a normalized difference for the terms. Do consider the explicit triple product integral is actually 6-way symmetric and not all directions of symmetry are being tested.

$$\varepsilon_{\text{symmetry}} = \frac{|C_{k,l,m} - C_{l,k,m}|}{\frac{1}{2}(|C_{k,l,m}| + |C_{l,k,m}|)} \quad (5.1)$$

$N_r$	Error	$N_r$	Error
3	1.43e-14	10	8.70e-06
4	2.30e-14	11	9.08e-04
5	1.76e-11	12	9.00e-03
6	1.12e-10	13	2.79e-01
7	7.68e-09	14	2.08e0
8	2.73e-08	15	2.74e0
9	9.96e-07		

**Table 5.2:** Highest error in the symmetric relation for this implementation of the Laguerre explicit triple product integral. The highest error is computing one fixed order and going over the other modes up to 15. The first 4 orders are not included, because they are close to machine precision

It is not immediately clear when looking at the errors how far off the results are, especially, if the precision of the literature is taken into account. The problem with this error presentation is that the actual values may be small but result in a large normalized error. What can be said about the error is that is not close to the machine error and that there is a clear trend with respect to the order of the method.

# Chapter 6

## Conclusion and Recommendation

The objective of this research was to implement cutting-edge numerical methods to model the effect on the wake of state-of-the-art control techniques with Ainslie's wake model. This chapter is divided into two sections. The first, section 6.1, is dedicated to answering the research questions and providing a general conclusion. The second, section 6.2, provides suggestions and considerations for future research work.

### 6.1 Conclusion

The research presented, was aimed at finding faster numerical methods for axisymmetric wake modeling, hopefully, speeding up medium-fidelity flow calculations. Fundamental to the choices made in this research is the possible future extension to wake control techniques. The chosen wake model was Ainslie's wake model, from which a slightly different set of governing equations has been derived to better fit the simulation. These governing equations have been solved with Laguerre functions in the radial direction and piecewise linear basis functions in a marching scheme for the axial direction.

Although the simulation converged with results, the accompanying conservation error is unusually high and may stem from different origins. The first error confronted came from the computing of the Laguerre explicit triple product integral. The limited implementation of these explicit expressions hinders research into higher-order modes in the simulation.

On a similar note, a strong correlation was found between the error and the relative number of radial modes between the inflow and the domain. This was most apparent for the full model since the error was immediately present behind the wind turbine with a higher starting error similar to the highest error achieved with the diffusion equation.

The method explored shows promising performance, yet whether its application

will be realized in future wake models, depends heavily on how well its drawbacks can be mitigated. Some of these drawbacks can be alleviated with further research and improved implementation. The current model facilitates an initial review of the method for wake modeling, specifically, with respect to the velocity profile and computation costs. These are the targets set in the chapter 1.

In the current phase, the model only supports wake modeling of standard wind turbine operations. None of the wake control techniques have been implemented and the model requires additional development to be able to do so. Depending on which wake control technique is to be implemented, the model should include either time-dependency for the modeling of DIC or time- and azimuthal-dependency for the modeling of DIPC. Additionally, the implementation of a prescribed eddy-viscosity demands revision too. The current eddy-viscosity is based on empirical fits to the outcomes of standard wind turbine operations and leads to wake dissipation for this implementation. Turbulence properties for the wake control techniques will correspond to vastly different eddy-viscosity models.

Laguerre functions come with some unique implementation problems, however, whether these complications are critical depends on what is required. Arguably, for the inflow velocity profile of this flow case, Laguerre functions form a poor fit. However, if the error at the start of the domain is considered satisfactory and the system has access to higher modes than those used in this research, the results may be more satisfactory. Linear cases where the truncation error is not reached so rapidly would form better modeling cases for the Laguerre basis functions.

Optimizing the script has been left out of the scope of this research. For a system with as highest order 15 and prescribed eddy viscosity, the computational time is approximately  $0.2[s]$ . Computing the eddy viscosity for each step, on the other hand, proves to be a costly effort, costing  $519.47[s]$ . Calculating the velocity field from the superposition of radial basis functions to find the minimum velocity and wake radius for the viscosity equation, is what costs the most computational power in the current implementation. The computational cost could be reduced by omitting the modeling of the full domain at every step and reducing the number of grid points in the velocity field for this calculation.

Comparing the results to those of other wake velocity deficit models or existing wake velocity deficit data, would not be productive with the current results. The dissipation of the velocity deficit is overestimated and makes serious comparison useless. Consequently, any substantial claims regarding accuracy would be unfounded.

## 6.2 Recommendations

The research was directed most toward the numerical aspect of the modeling of the equation behind the wind turbine. The implementation of the vorticity representation done as a replacement of the Reynolds shear stresses leaves for much potential improvement. Due to the distinctiveness of this particular numerical method, most empirically fitted viscosity equations do not make sense for unbounded basis functions. No empirically fitted viscosity expressions exist yet for the wakes of collective pitch control and individual pitch control. This means that for future implementations concerning wake control techniques, it will be beneficial to take up the shear stresses in the model.

Regarding the implementational issues of the Laguerre basis functions, it is recommended to find alternative ways of expressing the explicit triple Laguerre integrals. The work by Gillis and Shimshoni [1962] has a recurrence relationship (equation 33), which potentially could be combined with another explicit formula (equation 17) into a less error-prone method. Methods to compute the values of this equation with higher precision could be a solution too. The latter option will be computationally more expensive than the former.

This research, although it has encompassed more than one unbounded kind of basis function, has not produced a function that is easily fitted to the inflow condition. For these conditions, there could be better alternatives, which prove more straightforward to implement. If Laguerre functions are applied nonetheless, efforts to find more applicable scaling parameters may improve the fit.

On a similar note, the application of Laguerre functions or Hermite functions shows severe ill-conditioning for higher orders according to prof. Daniele Funaro<sup>3</sup>. Application of these functions is easier motivated, when, the equations form the steady-state solution to the problem, such as in the work of Funaro and Manzini [2021].

Provided this research had a limited time frame, there was no time budget left to match inflow conditions and viscosity inputs to available implementations of a similar wake model. This could provide additional insights into the relative differences between the different numerical implementations and could point out significant differences. Specifically, when comparing wake velocity profiles.

---

<sup>3</sup>From a personal response by prof. Daniele Funaro to questions regarding his work on pseudospectral Laguerre functions

[This page is intentionally left blank]

# Appendix A

## The One-Equation System

There is one key difference in the implementation of the substitution and that is the  $V(x, r) \frac{\partial U(x, r)}{\partial r}$ -term. Equation (3.7) can be worked-out to come to the matrix notation:

$$V(x, r) = \frac{1}{r} \begin{bmatrix} 1 - \psi_0(r) \\ 1 - \psi_1(r) \\ \vdots \\ 1 - \psi_{N_r}(r) \end{bmatrix} \underbrace{\begin{bmatrix} 1 & -2 & 2 & -2 & 2 \\ & 1 & -2 & 2 & -2 \\ & & 1 & -2 & 2 \\ \mathbf{0} & & & \ddots & \vdots \\ & & & & 1 \end{bmatrix}}_{\mathbf{A}} \begin{bmatrix} \frac{\partial U_0(x)}{\partial x} \\ \frac{\partial U_1(x)}{\partial x} \\ \vdots \\ \frac{\partial U_{N_r}(x)}{\partial x} \end{bmatrix} \quad (\text{A.1})$$

Leading to the integral expression for  $V(x, r) \frac{\partial U(x, r)}{\partial r}$ :

$$\iint_{\Omega} V(x, r) \frac{\partial U(x, r)}{\partial r} dV = \int_0^{\infty} \sum_{k,q=0}^{N_r} \frac{1}{r} \psi_m \psi'_k u_k (1 - \psi_q) A \begin{bmatrix} \frac{\partial U_0(x)}{\partial x} \\ \frac{\partial U_1(x)}{\partial x} \\ \vdots \\ \frac{\partial U_{N_r}(x)}{\partial x} \end{bmatrix} r dr dx \quad (\text{A.2})$$

Unlike for the method described in chapter 3, this expression is described in matrix notation and solved in that manner too. The derivative described by equation (2.47) can also be expressed in a matrix. The matrix expression and the resultant expression:

$$\sum_k^N \psi'_k(r) u_k(x) = \begin{bmatrix} \psi_0(r) \\ \psi_1(r) \\ \vdots \\ \psi_{N_r}(r) \end{bmatrix}^T \underbrace{\begin{bmatrix} 1 & 2 & 2 & 2 & 2 \\ & 1 & 2 & 2 & 2 \\ & & 1 & 2 & 2 \\ & & & \ddots & \vdots \\ & & & & 1 \end{bmatrix}}_{\mathbf{B}} \begin{bmatrix} u_0(x) \\ u_1(x) \\ \vdots \\ u_{N_r}(x) \end{bmatrix} \quad (\text{A.3})$$

$$\int_{x_l}^{x_r} \int_0^\infty \psi_m \begin{bmatrix} \psi_0(r) \\ \psi_1(r) \\ \vdots \\ \psi_{N_r}(r) \end{bmatrix}^T \mathbf{B} \begin{bmatrix} u_0(x) \\ u_1(x) \\ \vdots \\ u_{N_r}(x) \end{bmatrix} \begin{bmatrix} 1 - \psi_0 \\ 1 - \psi_1 \\ \vdots \\ 1 - \psi_{N_r} \end{bmatrix}^T \mathbf{A} \begin{bmatrix} \frac{\partial u_0(x)}{\partial x} \\ \frac{\partial u_1(x)}{\partial x} \\ \vdots \\ \frac{\partial u_{N_r}(x)}{\partial x} \end{bmatrix} r \, dr \, dx \quad (\text{A.4})$$

Applying the transpose to the left three terms results in a isolated term dependent of  $r$  that can be integrated and be treated as a single matrix:

$$\int_0^\infty \psi_m \left( \begin{bmatrix} \psi_0(r) \\ \psi_1(r) \\ \vdots \\ \psi_{N_r}(r) \end{bmatrix}^T \mathbf{B} \begin{bmatrix} u_0(x) \\ u_1(x) \\ \vdots \\ u_{N_r}(x) \end{bmatrix} \right)^T \begin{bmatrix} 1 - \psi_0 \\ 1 - \psi_1 \\ \vdots \\ 1 - \psi_{N_r} \end{bmatrix}^T \mathbf{A} \begin{bmatrix} \frac{\partial u_0(x)}{\partial x} \\ \frac{\partial u_1(x)}{\partial x} \\ \vdots \\ \frac{\partial u_{N_r}(x)}{\partial x} \end{bmatrix} r \, dr$$

$$\begin{bmatrix} u_0(x) \\ u_1(x) \\ \vdots \\ u_{N_r}(x) \end{bmatrix}^T \mathbf{B}^T \underbrace{\int_0^\infty \begin{bmatrix} \psi_0(r) \\ \psi_1(r) \\ \vdots \\ \psi_{N_r}(r) \end{bmatrix} \psi_m \begin{bmatrix} 1 - \psi_0 \\ 1 - \psi_1 \\ \vdots \\ 1 - \psi_{N_r} \end{bmatrix}^T r \, dr}_{\delta_{k,m} - C_{k,q,m}} \mathbf{A} \begin{bmatrix} \frac{\partial u_0(x)}{\partial x} \\ \frac{\partial u_1(x)}{\partial x} \\ \vdots \\ \frac{\partial u_{N_r}(x)}{\partial x} \end{bmatrix} \quad (\text{A.5})$$

The final result of the expression in vector notation:

$$\mathbf{u}^T \underbrace{\mathbf{B}^T ([\delta_{k,m}] - [C_{k,q,m}])}_{\mathbf{E}} \mathbf{A} \frac{\partial \mathbf{u}}{\partial x} \quad (\text{A.6})$$

The other terms in the momentum equation remain unaffected and this expression can be directly substituted to half the rank of the system. This comes with a computational

advantage, moreover, the mass equation will be satisfied pointwise. The pointwise satisfied continuity will impose a higher stiffness on the system, meaning smaller stepsizes are required. The disadvantage of the substitution is that the radial velocity is fixed to a piecewise constant discretization.

[This page is intentionally left blank]

# Appendix B

## Hermite Spline Implementation

An alternative to the finite element piecewise linear basis functions could be cubic Hermite splines. The cubic Hermite splines are visualised in figure B.1 and the equations that form the basis are displayed in equation (B.1).

Implementing cubic Hermite splines would lead to a higher-order Hilbert space ( $H^3$ ). This would yield a higher-order downstream discretization, which would not just be a positive for the overall level of continuity for the problem, but would lead to a higher-order substitution too.

$$\begin{aligned}h_{00}(t) &= 2t^3 - 3t^2 + 1 \\h_{10}(t) &= t^3 - 2t^2 + t \\h_{01}(t) &= -2t^3 + 3t^2 \\h_{11}(t) &= t^3 - t^2\end{aligned}\tag{B.1}$$

The domain  $t$  used in the cubic Hermite spline equation is defined piecewise (equation (B.2)). Keeping a uniform grid size distribution, the distance between the grid points can be simplified to  $\Delta x = x_k - x_{k-1}$ . The governing equations are still defined for the  $x$ -domain, thus requiring a transformation (equation (B.3)).

$$t = \frac{x - x_{k-1}}{x_k - x_{k-1}}\tag{B.2}$$

$$dx = \Delta x dt\tag{B.3}$$

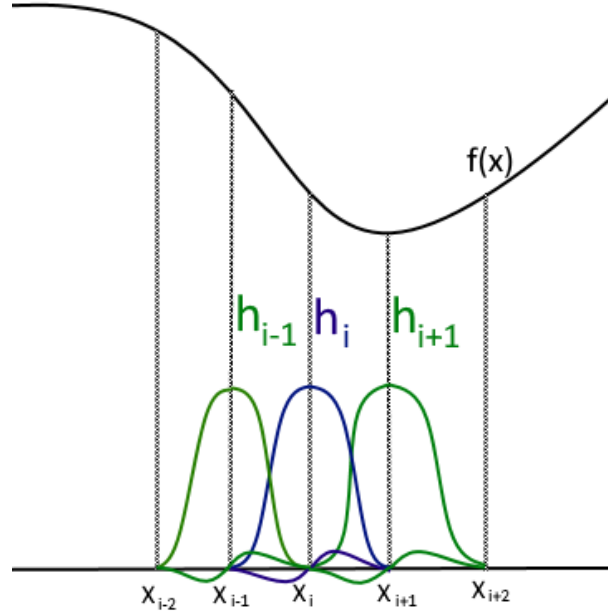


Figure B.1: Schematic of cubic Hermite spline finite element discretization.

## B.1 Hermite Spline Marching

Considering only the marching scheme, an axial velocity element will be discretized as such:

$$u(x) = \begin{cases} u_k h_{01}(t) - u_k h_{00}(t), & \text{if } x \geq x_{k-1} \ \& \ x < x_k \\ u'_k h_{10}(t) - u'_k h_{11}(t), & \text{if } x \geq x_k \ \& \ x \leq x_{k+1} \\ 0, & \text{otherwise } x < x_{k-1} \ \text{or } x \geq x_{k+1} \end{cases} \quad (\text{B.4})$$

The integral of the terms can be computed straightforwardly and does not require approximation techniques. This can be done by hand, it may be helpful to know that Matlab's symbolic toolbox is also able to solve these integrals exactly. Outcomes of the integrals can be tabulated and retrieved when required.

What will lead to the most noteworthy change is the change in the projection function, which now contains a vector of two functions in a vector:

$$b(t, r) = \psi_m(r) \begin{pmatrix} h_{01}(t) \\ h_{11}(t) \end{pmatrix} \quad (\text{B.5})$$

With this vector projection the final matrix is of the shape  $2 \times 2$  for the axial discretization, which matches the two unknowns  $u_r$  and  $u'_r$ .

## B.2 Hermite Spline Finite Elements

The velocity following the Ritz-Galerkin with a FE downstream direction. For now, the velocity is taken to be independent of the radial direction, and the azimuthal direction:

$$U(r, x) = U_\infty - \sum_{q=0}^{N_x} \begin{pmatrix} h_{00}u_q \\ h_{01}u'_q \\ h_{10}u_q \\ h_{11}u'_q \end{pmatrix} \quad (\text{B.6})$$

$$V(r, x) = \sum_{q=0}^{N_x-1} \begin{pmatrix} h_{00}v_q \\ h_{01}v'_q \\ h_{10}v_q \\ h_{11}v'_q \end{pmatrix} \quad (\text{B.7})$$

For implementing the Ritz-Galerkin method, the basis functions are not required to be orthogonal only linear independent; thus, to achieve a squared matrix, the projection vector only exists of two elements:

$$b(x) = \sum_{i=0}^{N_x} \psi_k(r) \begin{pmatrix} h_{10} \\ h_{11} \end{pmatrix}_i \quad (\text{B.8})$$

There are only a few ways of arranging the functions for the governing equations. To keep the notation as clean as possible, the possible different outcomes of the downstream discretization are worked out in this section. To get the general case we consider the integral of  $b(x)$  and  $u(x)$ . Substituting the expressions from :

$$\int_0^L \sum_{q,i}^{N_x} b(x)u(x) dx = \int_0^L \sum_{q,i}^{N_x} \begin{pmatrix} h_{01}(t) \\ h_{11}(t) \end{pmatrix} \begin{pmatrix} h_{00}(t)u_q \\ h_{10}(t)u'_q \\ h_{01}(t)u_q \\ h_{11}(t)u'_q \end{pmatrix}^T dx \quad (\text{B.9})$$

From hereon ( $t$ ) is implied for the cubic Hermite splines to keep the equations readable. The outcome of this equation becomes:

$$\Delta x \int_0^L \sum_{q,i}^{N_x} \begin{bmatrix} [h_{00}]_q[h_{00} + h_{01}]_i + [h_{01}]_q[h_{00} + h_{01}]_i & [h_{10}]_q[h_{00} + h_{01}]_i + [h_{11}]_q[h_{00} + h_{01}]_i \\ [h_{00}]_q[h_{10} + h_{11}]_i + [h_{01}]_q[h_{10} + h_{11}]_i & [h_{10}]_q[h_{10} + h_{11}]_i + [h_{11}]_q[h_{10} + h_{11}]_i \end{bmatrix} \begin{pmatrix} u_q \\ u'_q \end{pmatrix} dt$$

This outcome does not yet take into account the piecewise-defined property of the functions. There are three general cases where the result is not zero. Those are when  $q = i$ ,  $q = i - 1$ , and  $q = i + 1$ . Additionally, the elements at the start of the domain  $x = 0$  and at the end of the domain  $x = L$  will produce different matrices too.

The first case analyzed is when  $q = i$ . The resultant matrix becomes:

$$\zeta_{q,q} = \Delta x \int_0^L \begin{bmatrix} h_{00}[h_{00} + h_{10}] & h_{10}[h_{00} + h_{10}] \\ h_{01}[h_{10} + h_{11}] & h_{11}[h_{10} + h_{11}] \end{bmatrix} \begin{pmatrix} u_q \\ u'_q \end{pmatrix} dt$$

The case of  $q = i - 1$  reads:

$$\zeta_{q,q+1} = \Delta x \int_0^L \begin{bmatrix} 0 & 0 \\ h_{00}[h_{01} + h_{11}] & h_{10}[h_{01} + h_{11}] \end{bmatrix} \begin{pmatrix} u_q \\ u'_q \end{pmatrix} dt$$

Finally, the last matrix for  $q = i + 1$

$$\zeta_{q,q-1} = \Delta x \int_0^L \begin{bmatrix} [h_{01}][h_{00} + h_{10}] & [h_{11}][h_{00} + h_{10}] \\ 0 & 0 \end{bmatrix} \begin{pmatrix} u_q \\ u'_q \end{pmatrix} dt$$

The final two cases to consider are the two boundaries of the x-domain. The boundary conditions are Dirichlet boundary conditions at the start of the domain, fixing  $u_0$  and  $v_0$ . Similarly, at the end of the x-domain homogeneous Neumann boundary conditions are imposed, with the discretization choices made, explicitly fixing  $u'_{N_x-1}$  and  $v'_{N_x-1}$ .

The discretization at the boundary of the domain is schematically shown in section 2.3.1. The first element ranges from a virtual  $x_{-1}$  to  $x_1$ . In fact, only the functions above  $x_0$  are considered. Meaning the projection vector is different for this element. Similarly, the projection vector for the last element is different. The two vectors  $b_0$  and  $b_{N_x-1}$  are:

$$b_0 = \begin{pmatrix} 0 \\ h_{01} + h_{11} \end{pmatrix} \quad b_{N_x} = \begin{pmatrix} h_{00} + h_{10} \\ 0 \end{pmatrix} \quad (\text{B.10})$$

Applying this projection at the start of the domain leads to two unusual expressions:

$$\begin{aligned} \zeta_{0,0} &= \Delta x \int_0^1 \begin{bmatrix} 0 & 0 \\ h_{01}[h_{10} + h_{11}] & h_{11}[h_{10} + h_{11}] \end{bmatrix} \begin{pmatrix} u_q \\ u'_q \end{pmatrix} dt \\ \zeta_{0,1} &= \Delta x \int_0^1 \begin{bmatrix} 0 & 0 \\ h_{00}[h_{01} + h_{11}] & h_{10}[h_{01} + h_{11}] \end{bmatrix} \begin{pmatrix} u_q \\ u'_q \end{pmatrix} dt \end{aligned} \quad (\text{B.11})$$

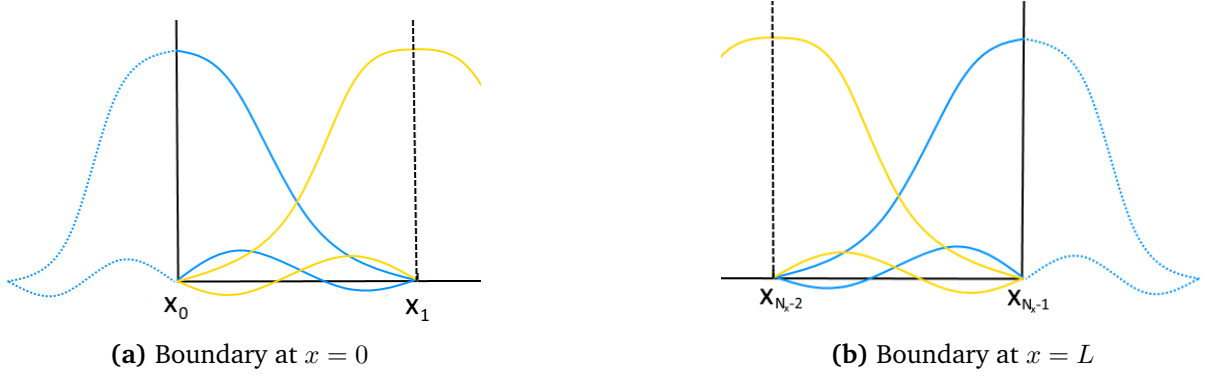


**Figure B.2:** The schematics of the boundaries for the FE discretization. The basis functions used for the FE approach are the cubic Hermite splines.

Similarly, at the end of the domain with its own different projection vector. The matrices become:

$$\begin{aligned}
 \zeta_{N_x-1, N_x-1} &= \Delta x \int_0^1 \begin{bmatrix} h_{00}[h_{00} + h_{10}] & h_{10}[h_{00} + h_{10}] \\ 0 & 0 \end{bmatrix} \begin{pmatrix} u_q \\ u'_q \end{pmatrix} dt \\
 \zeta_{N_x-1, N_x-2} &= \Delta x \int_0^1 \begin{bmatrix} [h_{01}][h_{00} + h_{10}] & [h_{11}][h_{00} + h_{10}] \\ 0 & 0 \end{bmatrix} \begin{pmatrix} u_q \\ u'_q \end{pmatrix} dt
 \end{aligned} \tag{B.12}$$

Consequently, the top row exists exclusively of zeros and the bottom row too. Meaning the top and bottom rows can be excluded from the system altogether. The combined system matrix (equation (B.13)) is of the size  $2N_x - 2 \times 2N_x - 2$ .

$$\mathcal{H} = \begin{bmatrix} \zeta_{0,0} & \zeta_{0,1} & 0 & & \dots & & 0 \\ \zeta_{1,0} & \zeta_{1,1} & \zeta_{1,2} & & & & \\ 0 & \zeta_{1,0} & \zeta_{1,1} & \zeta_{1,2} & & & \\ \vdots & & & & \ddots & & \vdots \\ & & & & & \zeta_{N_x-2, N_x-3} & \zeta_{N_x-2, N_x-2} & \zeta_{N_x-2, N_x-1} \\ 0 & & & & \dots & 0 & \zeta_{N_x-1, N_x-2} & \zeta_{N_x-1, N_x-1} \end{bmatrix} \tag{B.13}$$

Including the boundary conditions will allow for the separation of the first and last columns of the matrix. Leading to the final expression for the downstream discretization:

$$\mathcal{H}U = \mathcal{H}_{int}U_{int} + \mathcal{H}_{BC}U_{BC} \tag{B.14}$$

With the velocity vector and the boundary condition vector ( $U_{BC}$ ):

$$U_{int} = - \begin{pmatrix} u'_0 \\ u_1 \\ u'_1 \\ \vdots \\ u'_{N_x-1} \\ u_{N_x} \end{pmatrix}, U_{BC} = - \begin{pmatrix} u_{0,0} \\ u'_{N_x} \end{pmatrix} \quad (\text{B.15})$$

There will be cases for which the cubic Hermite splines are subjected to a differentiation with respect to  $x$ . Following the transformation of the  $t$ -domain to the  $x$ -domain by equation(B.3), the following is true:

$$\begin{aligned} \frac{dt}{dx} &= \frac{1}{\Delta x} \\ \frac{dh(t)}{dx} \frac{dt}{dt} &= \frac{dh(t)}{dt} \frac{dt}{dx} \\ \frac{dh(t)}{dx} &= \frac{dh(t)}{dt} \frac{1}{\Delta x} \end{aligned} \quad (\text{B.16})$$

Cancelling out the  $\Delta x$  in the previous expression.

# Bibliography

- A. S. Adams, D. W. Keith, C. Galinos, N. Dimitrov, T. J. Larsen, A. N., and K. S. Hansen. Mapping wind farm loads and power production - a case study on horns rev 1. *J. Phys.: Conf*, Ser. 753 032010, 2016. doi: 10.1088/1742-6596/753/3/032010.
- I. Afgan, J. McNaughton, S. Rolfo, D. D. Apsley, T. Stallard, and P. Stansby. Turbulent flow and loading on a tidal stream turbine by les and rans. *International Journal of Heat and Fluid Flow*, 43:96–108, 10 2013. ISSN 0142-727X. doi: 10.1016/J.IJHEATFLUIDFLOW.2013.03.010.
- J. F. Ainslie. Calculating the flowfield in the wake of wind turbines. *Journal of Wind Engineering and Industrial Aerodynamics*, 27, 1988. ISSN 01676105. doi: 10.1016/0167-6105(88)90037-2.
- J. D. Anderson. *Fundamentals of Aerodynamics*. McGraw-Hill series in aeronautical and aerospace engineering. McGraw-Hill Education, 2017. ISBN 978-1-259-12991-9.
- C. L. Archer and A. Vassel-Be-Hagh. Wake steering via yaw control in multi-turbine wind farms: Recommendations based on large-eddy simulation. *Sustainable Energy Technologies and Assessments*, 33:34–43, 6 2019. ISSN 2213-1388. doi: 10.1016/J.SETA.2019.03.002.
- G. B. Arfken, H. J. Weber, and F. E. Harris. Mathematical methods for physicists. *Mathematical Methods for Physicists*, 2013. doi: 10.1016/C2009-0-30629-7.
- S. Auluck. On the integral of the product of three bessel functions over an infinite domain. *The Mathematica Journal*, 14, 2012. doi: 10.3888/TMJ.14-15.
- C. Bak, F. Bitsche, R. Kim, T. Yde, A. Henriksen, L. C. Hansen, J P A A Gaunaa, and M Natarajan. The dtu 10-mw reference wind turbine. Technical report, DTU Wind Energy, 2013.
- R. J. Barthelmie and L. E. Jensen. Evaluation of wind farm efficiency and wind turbine wakes at the Nysted offshore wind farm. *Wind Energy*, 13(6):573–586, 2010. ISSN 1099-1824. doi: 10.1002/we.408.

- URL <https://onlinelibrary.wiley.com/doi/abs/10.1002/we.408>. eprint: <https://onlinelibrary.wiley.com/doi/pdf/10.1002/we.408>.
- T. Burton, N. Jenkins, D. Sharpe, and E. Bossanyi. *Wind Energy Handbook, Second Edition*. John Wiley and Sons, 5 2011. ISBN 9780470699751. doi: 10.1002/9781119992714. URL <https://onlinelibrary.wiley.com/doi/book/10.1002/9781119992714>.
- CAT. State of climate action 2022 — climate action tracker, 10 2022. URL <https://climateactiontracker.org/publications/state-of-climate-action-2022/>.
- H. Choi and P. Moin. Grid-point requirements for large eddy simulation: Chapman's estimates revisited. *AIP publishing*, 2011.
- International Electrotechnical Commission. Iec 61400-1:2019 — iec webstore — rural electrification, wind power, 2019. URL <https://webstore.iec.ch/publication/26423>.
- Wind Europe. Wind energy in europe: 2021 statistics and the outlook for 2022-2026, 2 2022.
- J. A. Frederik, B. M. Doekemeijer, S. P. Mulders, and J. W. van Wingerden. The helix approach: Using dynamic individual pitch control to enhance wake mixing in wind farms. *Wind Energy*, 23:1739–1751, 8 2020a. ISSN 1099-1824. doi: 10.1002/WE.2513. URL <https://onlinelibrary.wiley.com/doi/full/10.1002/we.2513><https://onlinelibrary.wiley.com/doi/abs/10.1002/we.2513><https://onlinelibrary.wiley.com/doi/10.1002/we.2513>.
- J. A. Frederik, R. Weber, S. Cacciola, F. Campagnolo, A. Croce, C. Bottasso, and J. W. Van Wingerden. Periodic dynamic induction control of wind farms: Proving the potential in simulations and wind tunnel experiments. *Wind Energy Science*, 5:245–257, 2 2020b. ISSN 23667451. doi: 10.5194/WES-5-245-2020.
- D. Funaro and G. Manzini. Stability and conservation properties of hermite-based approximations of the vlasov-poisson system. *Journal of Scientific Computing*, 88:1–36, 7 2021. ISSN 15737691. doi: 10.1007/S10915-021-01537-5/METRICS. URL <https://link.springer.com/article/10.1007/s10915-021-01537-5>.
- J. Gillis and M. Shimshoni. Triple product integrals of laguerre functions. *American Mathematical Society*, 16, 1962. URL <https://www.jstor.org/stable/2003810>.
- H. Glauert. Airplane propellers. *Aerodynamic Theory*, pages 169–360, 1935. doi: 10.1007/978-3-642-91487-4\_3.

- D. Gottlieb and S. A. Orszag. Numerical analysis of spectral methods. *Numerical Analysis of Spectral Methods*, 1 1977. doi: 10.1137/1.9781611970425. URL <https://epubs.siam.org/terms-privacy>.
- O. Gözcü and D. R. Verelst. The effects of blade structural model fidelity on wind turbine load analysis and computation time. *Wind Energy Science*, 5:503–517, 4 2020. ISSN 23667451. doi: 10.5194/WES-5-503-2020.
- T. Göçmen, P. van der Laan, P. E. Réthoré, A. P. Diaz, G. C. Larsen, and S. Ott. Wind turbine wake models developed at the technical university of Denmark: A review. *Renewable and Sustainable Energy Reviews*, 60:752–769, July 2016. ISSN 1364-0321. doi: 10.1016/j.rser.2016.01.113. URL <https://www.sciencedirect.com/science/article/pii/S136403211600143X>.
- M. F. Howland, J. Bossuyt, L. A. Martínez-Tossas, J. Meyers, and C. Meneveau. Wake structure in actuator disk models of wind turbines in yaw under uniform inflow conditions. *Journal of Renewable and Sustainable Energy*, 8:043301, 7 2016. ISSN 19417012. doi: 10.1063/1.4955091. URL <https://aip.scitation.org/doi/abs/10.1063/1.4955091>.
- G. Karniadakis and S. Sherwin. Spectral/hp element methods for computational fluid dynamics. *Spectral/hp Element Methods for Computational Fluid Dynamics*, 9 2005. doi: 10.1093/ACPROF:OSO/9780198528692.001.0001. URL <https://academic.oup.com/book/7538>.
- R. E. Keck, R. Mikkelsen, N. Troldborg, M. de Maré, and K. S. Hansen. Synthetic atmospheric turbulence and wind shear in large eddy simulations of wind turbine wakes. *Wind Energy*, 17:1247–1267, 8 2014. ISSN 1099-1824. doi: 10.1002/WE.1631. URL <https://onlinelibrary.wiley.com/doi/full/10.1002/we.1631><https://onlinelibrary.wiley.com/doi/abs/10.1002/we.1631><https://onlinelibrary.wiley.com/doi/10.1002/we.1631>.
- H. Kim, K. Kim, C. L. Bottasso, F. Campagnolo, and I. Paek. Wind turbine wake characterization for improvement of the ainslie eddy viscosity wake model. *Energies*, 11, 2018. ISSN 19961073. doi: 10.3390/EN11102823.
- J. Kirkwood. Mathematical physics with partial differential equations. *Mathematical Physics with Partial Differential Equations*, pages 1–478, 2 2018. doi: 10.1016/C2016-0-03724-5.
- T. J. Larsen, H. A. Madsen, G. C. Larsen, and K. S. Hansen. Validation of the dynamic wake meander model for loads and power production in the egmond aan zee wind

- farm. *Wind Energy*, 2012. doi: 10.1002/we.1563. URL <https://onlinelibrary.wiley.com/doi/10.1002/we.1563>.
- A. Leonard. Energy cascade in large-eddy simulations of turbulent fluid flows. *Advances in Geophysics*, 18:237–248, 1 1975. ISSN 0065-2687. doi: 10.1016/S0065-2687(08)60464-1.
- R. Malki, A. J. Williams, T. N. Croft, M. Togneri, and I. Masters. A coupled blade element momentum – computational fluid dynamics model for evaluating tidal stream turbine performance. *Applied Mathematical Modelling*, 37:3006–3020, 3 2013. ISSN 0307-904X. doi: 10.1016/J.APM.2012.07.025.
- D. Micallef, G. Van Bussel, C. S. Ferreira, and T. Sant. An investigation of radial velocities for a horizontal axis wind turbine in axial and yawed flows. *Wind Energy*, 16: 529–544, 2013. ISSN 10991824. doi: 10.1002/WE.1503.
- mpmath. mpmath - python library for arbitrary-precision floating-point arithmetic. URL <https://mpmath.org/>.
- W. Munters and J. Meyers. Dynamic strategies for yaw and induction control of wind farms based on large-eddy simulation and optimization. *Energies 2018, Vol. 11, Page 177*, 11:177, 1 2018. ISSN 1996-1073. doi: 10.3390/EN11010177. URL <https://www.mdpi.com/1996-1073/11/1/177/html><https://www.mdpi.com/1996-1073/11/1/177>.
- G. B. Picotto, R. Bellotti, and A. Sosso. Combining induction control and wake steering for wind farm energy and fatigue loads optimisation. *Journal of Physics: Conference Series*, 1037:032011, 6 2018. ISSN 1742-6596. doi: 10.1088/1742-6596/1037/3/032011. URL <https://iopscience.iop.org/article/10.1088/1742-6596/1037/3/032011><https://iopscience.iop.org/article/10.1088/1742-6596/1037/3/032011/meta>.
- F. Porté-Agel, Y. T. Wu, H. Lu, and R. J. Conzemius. Large-eddy simulation of atmospheric boundary layer flow through wind turbines and wind farms. *Journal of Wind Engineering and Industrial Aerodynamics*, 99, 2011. ISSN 01676105. doi: 10.1016/j.jweia.2011.01.011.
- I. Reinwardt, L. Schilling, P. Dalhoff, D. Steudel, and M. Breuer. Dwm model calibration using nacelle-mounted lidar systems. *European Academy of Wind Energy*, 2019.
- H. Schulte and E. Gauterin. Input-to-state stability condition for passive fault-tolerant control of wave and wind energy converters. *IFAC-PapersOnLine*, 48: 257–262, 2015. ISSN 24058963. doi: 10.1016/J.IFACOL.2015.09.537. URL

- [https://www.researchgate.net/publication/282008282\\_Input-to-State\\_Stability\\_Condition\\_for\\_Passive\\_Fault-Tolerant\\_Control\\_of\\_Wave\\_and\\_Wind\\_Energy\\_Converters](https://www.researchgate.net/publication/282008282_Input-to-State_Stability_Condition_for_Passive_Fault-Tolerant_Control_of_Wave_and_Wind_Energy_Converters).
- N. Sedaghatizadeh, M. Arjomandi, R. Kelso, B. Cazzolato, and M. H. Ghayesh. Modelling of wind turbine wake using large eddy simulation. *Renewable Energy*, 115: 1166–1176, 1 2018. ISSN 0960-1481. doi: 10.1016/J.RENENE.2017.09.017.
- J. Shen, T. Tang, and L. L. Wang. *Spectral Methods*, volume 41. Springer Berlin Heidelberg, 2011. ISBN 978-3-540-71040-0. doi: 10.1007/978-3-540-71041-7. URL <http://link.springer.com/10.1007/978-3-540-71041-7>.
- W. Z. Shen, R. Mikkelsen, J. N. Sørensen, and C. Bak. Tip loss corrections for wind turbine computations. *Wind Energy*, 8:457–475, 2005. ISSN 10954244. doi: 10.1002/WE.153.
- J. N. Sørensen and W. Z. Shen. Numerical modeling of wind turbine wakes. *Journal of Fluids Engineering*, 124:393–399, 6 2002. ISSN 0098-2202. doi: 10.1115/1.1471361. URL <https://asmedigitalcollection.asme.org/fluidsengineering/article/124/2/393/444521/Numerical-Modeling-of-Wind-Turbine-Wakes>.
- K. Thomsen and P. Sørensen. Fatigue loads for wind turbines operating in wakes. *Journal of Wind Engineering and Industrial Aerodynamics*, 80(1):121–136, March 1999. ISSN 0167-6105. doi: 10.1016/S0167-6105(98)00194-9. URL <https://www.sciencedirect.com/science/article/pii/S0167610598001949>.
- T. Uchida, T. Yoshida, M. Inui, and Y. Taniyama. Doppler lidar investigations of wind turbine near-wakes and les modeling with new porous disc approach. *Energies*, 14, 4 2021. ISSN 19961073. doi: 10.3390/EN14082101.
- D. van der Hoek, J. Frederik, M. Huang, F. Scarano, C. S. Ferreira, and J. W. Van Wingerden. Experimental analysis of the effect of dynamic induction control on a wind turbine wake. *Wind Energy Science*, 7:1305–1320, 6 2022. ISSN 23667451. doi: 10.5194/WES-7-1305-2022.
- L. J. Vermeer, J. N. Sørensen, and A. Crespo. Wind turbine wake aerodynamics. *Progress in Aerospace Sciences*, 39:467–510, 8 2003. ISSN 0376-0421. doi: 10.1016/S0376-0421(03)00078-2.
- D. C. Wilcox. *Turbulence modeling for CFD*. Griffin Printing, 2nd edition, 1994. ISBN 0-9636051-0-0.
- Wolfram. Wolfram mathematica: The world’s definitive system for modern technical computing. URL <https://www.wolfram.com/mathematica/>.